http://dx.doi.org/10.1016/j.ijplas.2017.01.004


# Anisotropic and asymmetrical yielding and its evolution in plastic deformation: Titanium tubular materials

Heng Li [a,*], Haiqin Zhang [a,b], He Yang [a,*], Minwang Fu[c], Heng Yang[b]
[a] State Key Laboratory of Solidification Processing, School of Materials Science & Engineering, Northwestern Polytechnical University, Xi'an, 710072, P.R. China
[b] Western Energy Material Technologies Co., LTD., Xi'an, 710016, P.R. China,
[c] Department of Mechanical Engineering, The Hong Kong Polytechnic University, Hung Hom, Kowloon, Hong Kong, P.R. China

*Corresponding authors: Email: liheng@nwpu.edu.cn (H. Li), yanghe@nwpu.edu.cn (H. Yang), Tel./Fax.: 86-29-88495632

## Abstract

The coupling effects of low asymmetry of HCP structure and transient non-uniform stress/strain states during multi-pass deformation processing cause a great variation in crystallographic orientation of titanium tubes, which may induce anisotropic/asymmetrical behaviors and affect the formability and service performance of the materials. The unique plastic deformation and mechanisms under 3D stress need to be accurately understood for integrated design of fabrication and forming of titanium tubular products via simultaneously achieving shape forming and property tailoring. How to address this eluded and tantalized issue, however, is still a bottleneck issue. In tandem with this, taking high strength titanium tube (HSTT) as a case, by using macro/meso scaled hybrid methodology, a correlation among loading condition, distorted plasticity and texture evolution of the material is established and articulated by the following: 1) Via Knoop indentation, tension/compression and EBSD, the distorted plasticity of HSTT is identified, and the combinations of three slip and two twinning modes are found to dominate the inhomogeneous deformation, which must be introduced in viscoplastic self-consistent (VPSC) crystal plasticity; 2) A compression-based orthogonal inverse method is used to calibrate the crystal plasticity parameters and validated from various aspects, and the VPSC-based computation is conducted for tubular materials with six typical initial textures under six fundamental loadings; 3) The remarkable distorted plasticity and evolution are observed for most cases; The interactions among slipping/slipping, slipping/twinning and twinning/twinning coordinate the anisotropic/asymmetrical behaviors and hence induce the distorted evolution of plasticity; The relationship between deformation modes (strain vectors) and texture evolution is constructed, and by allocating plastic flow in 3D space, the tubes with the desired textures and bespoke properties can be tailored in cold rolling.

**Keywords*:*** Anisotropy of what; Asymmetry of what; Viscoplastic self-consistent crystal

plasticity; Inhomogeneous deformation

## 1. Introduction

Titanium tubular materials have attracted increasing applications as one of the key high-performance and lightweight structures in many high-end clusters such as aerospace, marine, energy and healthcare (Yang et al. 2012; Banerjee and Williams, 2013). While, titanium tubular parts are manufactured by multi-pass thermal-mechanical fabrication processes such as extrusion, rolling, and many subsequent forming processes including bending, flaring, hydroforming and joining. Subjected to various loading conditions, complex tensile and compressive stress states are often induced. The inherently low asymmetry of HCP alpha titanium tube makes its behaviors strongly sensitive to three-dimensional (3D) stress state. Thus, the coupling effects of inherently low asymmetry of crystal structure and transient stress/strain states induce more inhomogeneous deformation (Rodríguez-Galán et al., 2015). Along with unequal deformation, diverse deformation modes further result in the preferred crystallographic reorientation, and the texture evolution then in turn enhances the inhomogeneous deformation and induces multiple tensile and compressive instabilities. Taking high strength Ti-3Al-2.5V tube (SAE, 2010) as an instance, the transient stress and strain states during the whole rolling process make titanium tube exhibit a great variation in crystallographic orientation, which affects the subsequent formability and service performance of the materials. Thus, for integrated design and development of both fabricating and forming processes for producing tubular products with high quality and satisfied properties, it is critically needed to establish the whole spectrum of knowledge of the deformation behaviors and mechanisms of titanium tube under complex stress states. However, for tubular materials, it is a challenge issue to characterize their plastic response under 3D stress states due to the limitation of circle and hollow structure (Kuwabara, 2007).

So far, great efforts have been provided for exploring the plastic deformation behaviors (including yielding, strain hardening and flow rule) and revealing the underlying mechanisms under different loading conditions (Deshpande et al., 2005; Banabic et al., 2010) for different kinds of materials by using in-situ/ex-situ TEM and atomistic/continuum modeling (Vitek et al., 2004; Wang and Beyerlein, 2011; Máthis et al., 2015). It is known that most polycrystalline materials such as FCC, BCC and HCP show pronounced anisotropic behaviors, viz., different strengths along stress symmetric line, as shown in Fig.1, which have been verified by the texture-induced dislocation mechanism (Barlat et al., 1997, 2003; Iadicola et al., 2008; Khan and Yu, 2012; Tuninetti et al., 2015). However, as shown in Fig.1, the anisotropy behaviors are

axial symmetry about the tension-compression (T-C) stress dividing line FL. In this case, the anisotropic plasticity and evolution in the first quadrant of stress plane, as shown in Fig.1, can be assumed to cover the entire behaviors in full stress state. In addition to the anisotropic responses, the other most notable feature is the asymmetry distribution along the T-C stress dividing line FL for many advanced materials even including FCC (Cheng et al., 2003; Cazacu and Barlat, 2004), which implies both the directionality sensitivity and pressure sensitivity occur simultaneously.

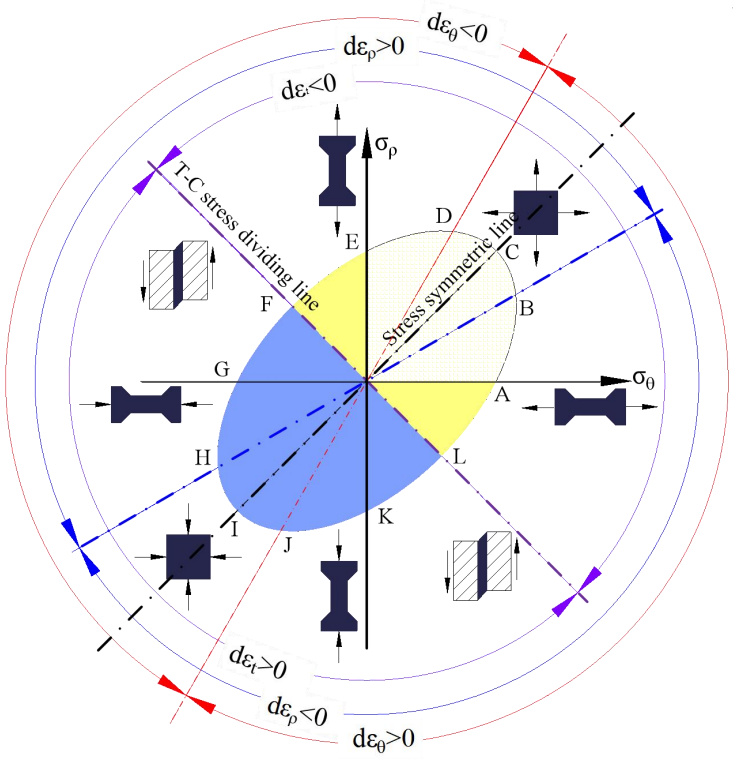


Note:

| | |
|---|---|
| Typical stress states: | $(\eta,\bar{\theta})$ |
| A - uniaxial tension | $(1/3,1)$ |
| B - plane strain | $(\sqrt{3}/3,0)$ |
| C - biaxial tension | $(2/3,-1)$ |
| D - plane strain | $(\sqrt{3}/3,0)$ |
| E - uniaxial tension | $(1/3,1)$ |
| F - shear | $(0,0)$ |
| G - uniaxial compression | $(-1/3,-1)$ |
| H - plane strain | $(-\sqrt{3}/3,0)$ |
| I - biaxial compression | $(-2/3,1)$ |
| J - plane strain | $(-\sqrt{3}/3,0)$ |
| K - uniaxial compression | $(-1/3,-1)$ |
| L - shear | $(0,0)$ |

$$\eta=\sigma_m/\bar{\sigma}\quad \cos[\frac{\pi(1-\bar{\theta})}{2}]=\frac{27}{2}\frac{J_3}{\sigma_m{}^3}$$

**Fig.1.** Stress and strain partitioning zones in plane stress condition.

Actually, both the anisotropy and asymmetry are common phenomena not only in plastic deformation but also in other deformations such as elastic deformation (Bauschinger effect), creep and phase transformation (Barlat et al., 2003; Tsuno et al., 2008; Raniecki and Mróz, 2008; Grolleau et al., 2011; Reedlunn et al., 2014). As mentioned before, the texture-induced dislocation mechanisms satisfy the directional sensitivity by initiating the Schmid law governed slipping. For the given preferred texture, the anisotropic behaviors can thus occur for most materials with FCC, BCC and HCP crystal structures. These pressure insensitive phenomena are attributed to the Schmid law governed slipping, which is a reversible shear mechanism. While, for the T-C asymmetry, the pressure sensitivity requires that the internal shear mechanism of deformation is sensitive to the sign of shear stress. Such irreversible mechanisms include twinning with polarity nature (Proust et al., 2009; Tuninetti, et al., 2015), directional slip such as

non-Schmid sliding and asymmetric slip (Lim et al., 2015; Wilson, 1975), porosity induced deformation (Drucker, 1973; Cazacu and Stewart, 2009) and internal stress related mechanisms such as phase transformation, temperature gradient, opening of micro crack, residual stress, internal Bauschinger effect, nonlinear solute-dislocation interaction and inhomogeneous plastic deformation (Wilson, 1975).

As shown in Fig. 2, it can be summarized that, for the materials with different crystal structures, the dominated plastic deformation mechanisms are different, which surely induces a certain degree of anisotropy and asymmetry. Since the contributions of porosity induced deformation and internal stress related mechanism on anisotropy and asymmetry seem similar for all types of materials with FCC, BCC or HCP structure, the roles of the Schmid slipping, twinning and Non-Schmid slipping are discussed in the following.

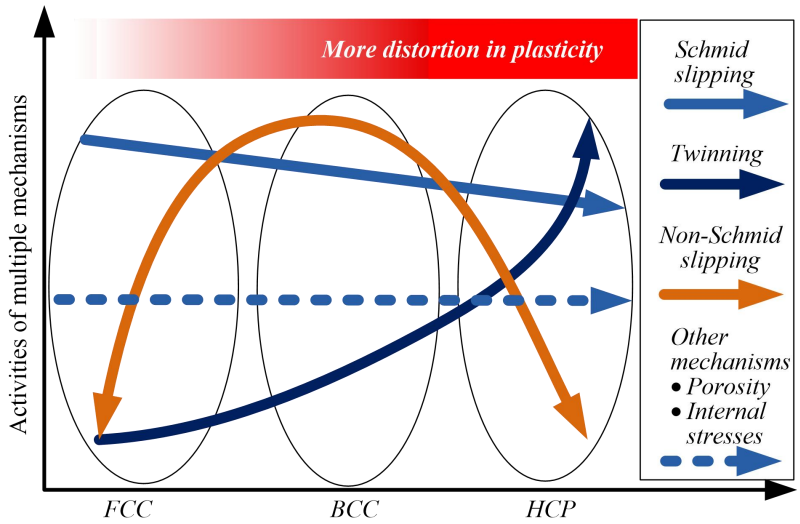


**Fig.2.** Schematic of the deformation map of materials with different crystal structures.

For FCC materials, there are enough Schmid slipping systems available for accommodating arbitrary deformation, and thus less twinning is needed, which results in the obvious anisotropy and the neglected asymmetry (Barlat et al., 1997). This is the reason why some strongly textured FCC materials exhibit remarkable anisotropy, while remain tension-compression (T-C) symmetry. However, at the extreme conditions such as cryogenic and dynamic environments or with special microstructures such as nanostructured and ultrafined grain metals, there is a substantial T-C asymmetry. For the former, twinning is a dominative mechanism, while for the latter, the asymmetry arises from the pressure dependence of the dislocation self-energy (Cheng et al., 2003: Tomar and Zhou, 2006).

As shown in Fig.2, for BCC materials, less but sufficient Schmid slipping is available for compatible deformation, and the twinning also becomes important under the extreme conditions of low temperature and high strain rate. While, some BCC materials such as Fe, Mo, Nb, Cu and

Ta, present the significant T-C asymmetry governed by the Non-Schmid effect, viz., non-glide stress associated with stress-state dependence of the Peierls barrier for screw dislocation (Jiao et al., 1996; Nitz et al., 1998; Gall et al., 1999; Ogata et al., 2002; Vitek et al., 2004; Tschopp and McDowell, 2007; Tsuno et al., 2008; Bassani and Racherla, 2011; Wang and Beyerlein, 2011; Patra et al., 2014). This pressure effect on Peierls glide stress can explain the minor T-C asymmetry of about 0.3% for pure Al with FCC structure (Bulatov et al., 1999). As shown in Fig.2, the T-C asymmetry of BCC materials is generally greater than that of FCC materials.

While, for HCP materials, the least slipping systems require twinning to accommodate plastic deformation, which causes the most significant anisotropy and asymmetry such as Mg-alloy (Stanford et al., 2012; Tari et al., 2014; Kabirian et al., 2015), Ti-alloy (Jones and Hutchinson, 1981; Graff et al., 2007; Khan et al., 2007; Nixon et al., 2010; Gilles et al., 2011; Revil-Baudard et al., 2014; Tuninetti et al., 2015) and other HCP materials (Mitsunobu et al., 2014). Based on the schematic of the deformation map shown in Fig.2, the superposition of anisotropy and asymmetry may result in distorted plasticity for these materials, viz., irregular yielding and nonlinear hardening in full stress space. However, this coupling effect has not been fully addressed yet.

As previously mentioned, to achieve high quality titanium tubular parts in both geometry accuracy and mechanical properties, it is critical to have a full understanding of the complex distorted plasticity and its evolution in deformation processes with different stress states. Unfortunately, different from bulk materials or thick sheets (Boger et al., 2005; Piao et al., 2012; Tuninetti, et al., 2015), tubular materials generally have geometrical non-linearity such as curved surfaces, except for the uniaxial tension along longitudinal direction. It is thus a challenge to obtain the plastic response along other directions. Meanwhile, it is thought that Schimid glide and twinning are two major directional mechanisms for HCP materials. Since the viscoplastic self-consistent polycrystal (VPSC) is capable for slip/twinning coordinated deformation predictions (Lebensohn et al., 1996; Styczynski et al., 2004; Agnew and Duygulu, 2005; Xu et al., 2008; Iadicola et al., 2008; Graff et al., 2007; Brown et al., 2012; Kabirian et al., 2015; Zhou et al.,2016), it is used in exploring the behaviors of titanium tubular materials in 3D stress state (Jeong et al., in press). While, the VPSC-based computation relies on the robust calibration of the mesoscaled parameters of crystal plasticity via dedicated experiments.

In this study, as shown in Fig.3, a macro/meso scaled hybrid methodology is used to establish a quantitative correlation between loading condition, distorted plasticity, texture evolution and mechanisms of high strength titanium tube (HSTT) in deformation processes. A near alpha HSTT is used as an instance of tubular materials. First, by using elaborately designed uniaxial

tension/compression experiments of tubular specimens and Electron Backscattered Diffraction (EBSD) analysis, the slip/twinning dominated multiple mechanisms of titanium are identified; Then, a compression-based orthogonal inverse method is used to calibrate the parameters of crystal plasticity model; Thirdly, the VPSC-based computation with the same set of crystal parameters is conducted for the tubes with six typical initial textures under six fundamental loading conditions denoted as *A*, *C*, *E*, *G*, *I* and *K* in Fig.1; Finally, the distorted plasticity and its evolution in full stress state as well as its physical mechanisms are articulated, and by establishing the correlation between loading condition and final texture, the idea to coordinate the deformation modes in 3D space for tailoring desired textures of HSTT is clarified for ensuring the needed properties of the deformed tubular products.

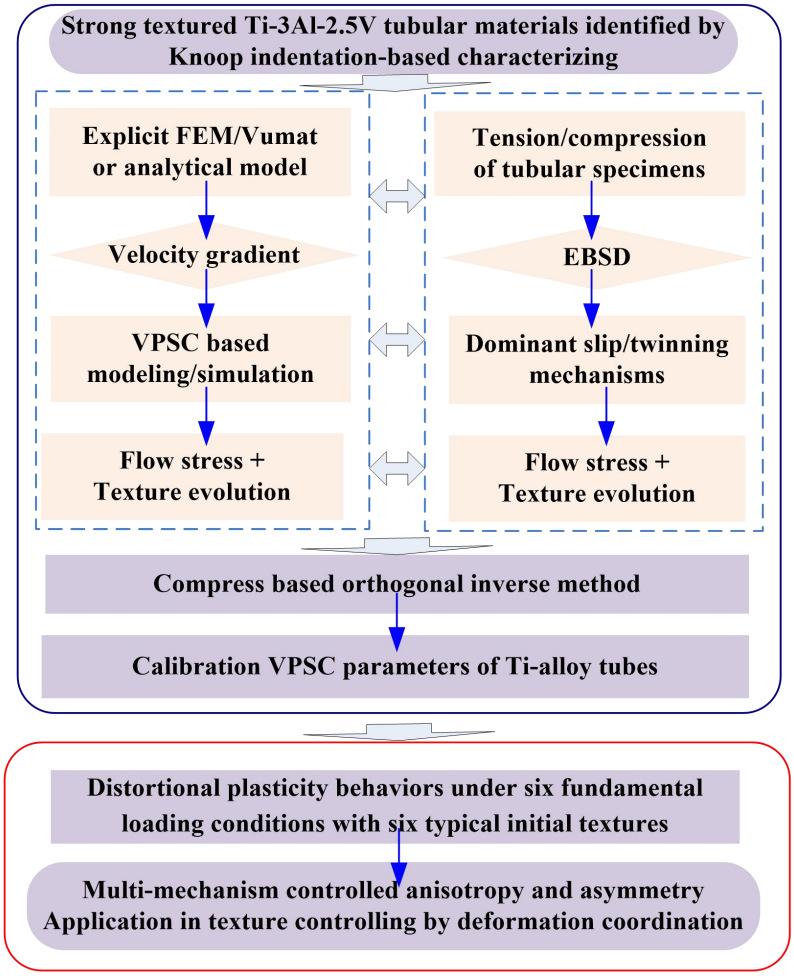


**Fig.3.** Macro/meso scaled hybrid methodology.

## 2. Experimental procedures

### *2.1 Case study materials*

The as-received material is the stress relieved Ti-3Al-2.5V titanium tube (SAE, 2010) with the dimensions of 12 mm × 0.9 mm (tube diameter × wall thickness). The morphology of this near

alpha tube is characterized by a large number of cold working produced alpha grains with minor beta phase spread out at the grain boundaries. The tested tubes are fabricated by hot extrusion, multi-pass cold rolling and interval annealing, and the final cold pilgering is believed to determine the final texture of HSTT. The major microstructure feature of the Ti-3Al-2.5V tubes is the diverse textures in the finished products even with the same geometrical dimensions.

### *2.2 Knoop indentation-based characterization of tubular materials*

Knoop microhardness tests are conducted to preliminarily estimate the overall anisotropy/ asymmetry coupled distorted plasticity of the as-received tubular material. Knoop indentation test is a standard method for material characterization due to the fact that they provide an easy, inexpensive, non-destructive and objective method for evaluating basic properties from small volumes of materials or thin-walled tubular materials, which are difficult to characterize (Zisis and Giannakopoulos, 2011). Why the Knoop indentation-based method can be used to evaluate the anisotropic characteristics of materials is essentially attributed to the non-centrosymmetric pyramid shape of the indenter, as shown in Fig.3, and the six hardness indentations on the three orthogonal planes along different directions, as shown in Fig.4 (Suwas et al., 2003). Based on the measured Knoop hardness data characterizing the strong anisotropy, how to analytically convert the hardness data into the stress data without losing the anisotropy information is another critical issue. Instead of using the Mises criterion, the Hill'48 yield criterion is introduced into the Knoop indentation-based procedure to more accurately calculate the stress in each indentation. By combining the stress data converted from the anisotropic hardness data, the yield locus of the anisotropic materials can thus be indirectly determined and estimated. A brief explanation of the improved Knoop indentation-based characterization method used for determination of the yield locus is presented below.

- Geometry of Knoop microhardness indenter and measuring locations for characterizing anisotropic and asymmetrical behaviors

As shown in Fig.4, the special pyramid shape of the Knoop indenter can produce a rhombohedral shaped indentation with the long and short diagonals with the ratio $\delta$ approximately 7:1. The indenter of Knoop is asymmetric with respect to the center point, and this non-centrosymmetric Knoop indenter reveals directionality in Knoop Hardness Value (KHV) on the three orthogonal planes, and hence the anisotropic deformation behavior of material. The other indenters like Brinell, Rock-well, or Vickers are not so sensitive to mechanical anisotropy due to the high degree of symmetry of the indenter. Fig.4 shows that the Knoop indenter has a longitudinal angle 172°30′ and a transverse angle of 130°0′. The

penetration depth of this indenter is approximately 1/30 of the long diagonal of the indentation. The geometry of the microindenter is designed in such a way that each facet of a pyramid indenter could produce a large compressive stress in a direction normal to the contact plane and a small frictional shear stress component parallel to the plane and in a downward direction. The compressive stress may be resolved into two parts: hydrostatic compressive stress and a deviatoric shear stress along the planes bisecting the direction parallel and normal to the indenter surface. The direction of the shear stress is a function of the geometry of indenter. The KHV is assumed to be representative of a stress deviator, which is determined by the indenter geometry.

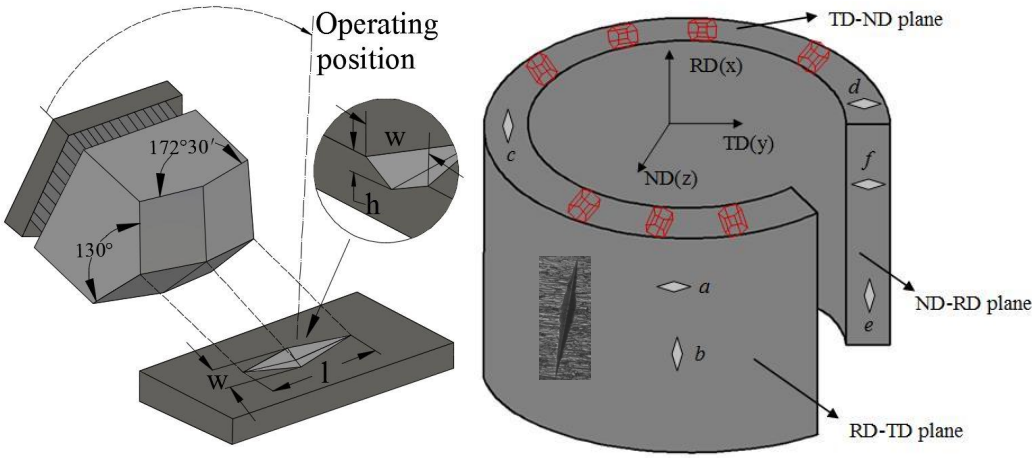


**Fig.4.** Knoop indenter and orientations of the Knoop indentations on three different planes.

As shown in Fig.5, two Knoop indentations were made on each of the three principal anisotropic planes (RD, TD and ND planes) with the indenter major axis aligned with the principal directions. The macroscopic coordinate system includes RD-rolling, TD-transverse and ND-through thickness directions. The resulted six orientations of indentation are marked as '*a*' to '*f*' on the three planes, and the six Knoop hardness values ('*a*'-'*f*') are graphically represented in Fig.5. In this study, as shown in Fig.5, the six Knoop indentations are selected for tubular materials.

- Mapping relationship between the stress points in the yield stress space and the six indentation locations in Knoop hardness tests

The graphical presentation of the Knoop indentation-based yield stress utilizes a planar representation of 3D space, and the planar representation is referred to as an octahedral plane, as shown in Fig.5. It is thought that the Knoop indenter orientation determines the directions on the octahedral strain plane. The directions of the six Knoop indentations ('a'-'f') are determined by the 7:1 strain-ratio associated with each of the six Knoop indenter orientations. The six indenter orientations are shown in Fig.5(a), and the octahedral strain plane is defined by $\varepsilon_1 + \varepsilon_2 + \varepsilon_3 = 0$,

as shown in Fig.5(b). **The coordinates of the six Knoop indentations ('a'-'f') in the octahedral strain plane and in the stress plane**. Taking the direction a as a case, the conversion from the indentation locations in Knoop hardness tests to the stress points in yield stress space is described in detail.

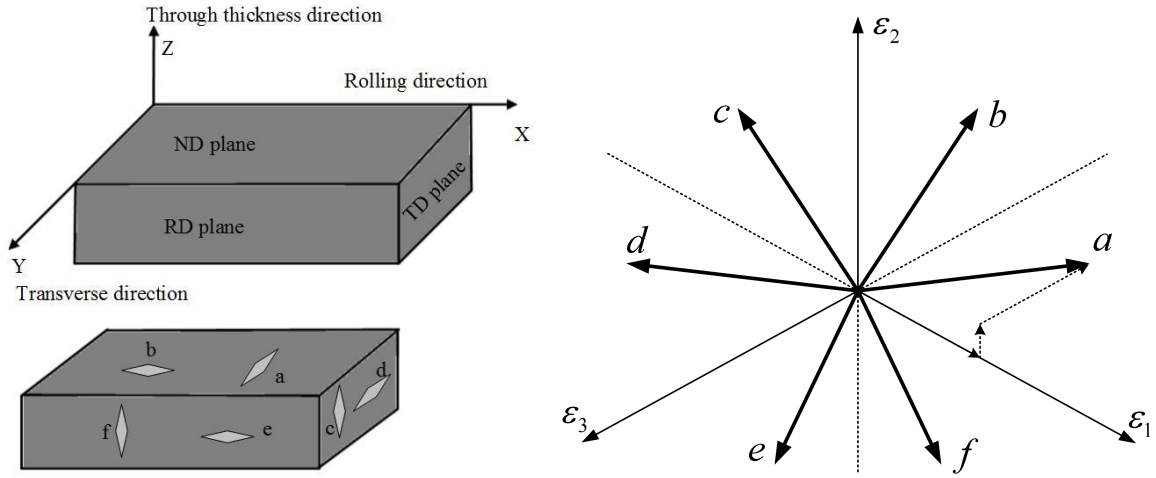


(a) (b)

**Fig.5** Directions of the six Knoop indentations ('a'-'f'): (a) for the microhardness test on three different planes; (b) in the octahedral plane.

As shown in Fig.5(b), the octahedral strain plane coordinates corresponding to the direction a are (7, 1, -8). The direction of a in octahedral strain plane is determined by consecutively drawing three lines parallel to the $\varepsilon_1$, $\varepsilon_2$, and $\varepsilon_3$ axes lines with 7, 1, and -8 units, respectively. A line from the origin through the ends of the third line is plotted, which indicates the direction a, as shown in Fig.5(b). Consequently, the directions of the six Knoop indentations ('a'-'f') are plotted in the octahedral strain plane shown in Fig.5(b).

By normalizing the coordinates corresponding to the octahedral strain plane as shown in Table 1, the directions of the six Knoop indentations ('a'-'f') are graphically represented in strain plane in Fig.6 (a). Based on the above analysis and the stress-strain relationship, we can obtain the qualitative directions of the six Knoop indentations in the stress space and shown in Fig.6(b). The plane yield locus of the as-received tubular material can then be plotted by converting the anisotropic Knoop hardness values to the yield stress.

**Table 1**. Conversion from the coordinates of the six Knoop indentations ('a'-'f') in the octahedral strain plane to the coordinates in the strain plane.

| Indentation Orientation | The coordinates in the octahedral strain plane | The coordinates in the strain plane |
|---|---|---|
| a | 7,1,-8 | 15,9 |
| b | 1,7,-8 | 9,15 |
| c | -8,7,1 | -9,6 |

| | | |
|---|---|---|
| d | -8,1,7 | -15,-6 |
| e | 1,-8,7 | -6,-15 |
| f | 7,-8,1 | 6,-9 |

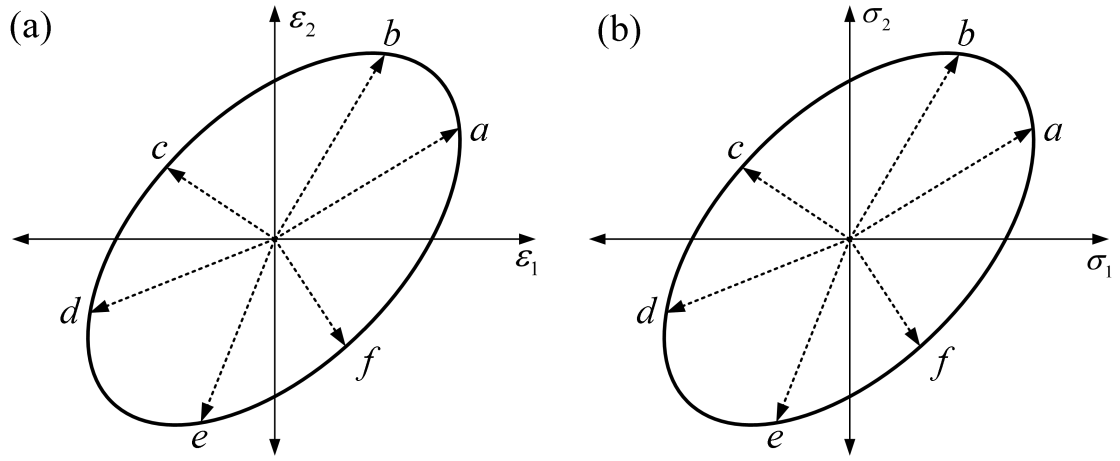


**Fig.6.** The directions of the six Knoop indentations ('a'-'f'): (a) by normalizing the strain-ratio; (b) in the stress plane.

- Formulation for converting the Knoop hardness to strength information

The foundation of the conversion is that the KHV is proportional to the shear stress on the octahedral plane. For plane stress condition, Eq. (1) shows the relationship between the KHV and the shear stress in the octahedral space established via many experiments and has been validated and applied (Wheeler and Ireland,1966; Amateau et al., 1975; Suwas et al., 2003; Mondal et al., 2013).

$$KHV \approx 3/\sqrt{2}\tau_8 = (\sigma_1^2 - \sigma_1\sigma_2 + \sigma_2^2)^{1/2} = (1 - \sigma_2/\sigma_1 + (\sigma_2/\sigma_1)^2)^{1/2}\sigma_1 = (1 - \sigma_1/\sigma_2 + (\sigma_1/\sigma_2)^2)^{1/2}\sigma_2 \quad (1)$$

With the relationship of $\sigma_2/\sigma_1 = \alpha_i$ (i=*a, b, c, d, e, f*) for each indentation position, the yield stress at each indentation can be determined:

$$\sigma_1 = KHV(1 - \alpha_i + \alpha_i^2)^{-1/2};\ \ \sigma_2 = KHV\alpha_i(1 - \alpha_i + \alpha_i^2)^{-1/2} \quad (2)$$

Instead of the Levy–Mises flow rule, the Hill'48 yield criterion is introduced into the Knoop indentation-based procedure to more accurately calculate the stress ratio $\alpha_i$. Since the tests along the hoop direction and radial direction are difficult to be conducted using tubular materials, only the uniaxial tension test is used and the normal anisotropy Hill'48 function is used and shown in Eq.(3).

$$f(\boldsymbol{\sigma}) = (\mathrm{G} + H)\sigma_1^2 - 2H\sigma_1\sigma_2 + (H + F)\sigma_2^2 - \sigma_m^2 \quad (3)$$

where $\sigma_m$ is the flow stress. *F*, *G*, and *H* are the anisotropy coefficients and determined by Eq.(4) in the following.

$$\begin{cases} F = (1/R_{22}^2 + 1/R_{33}^2 - 1/R_{11}^2)/2 \\ G = (1/R_{33}^2 + 1/R_{11}^2 - 1/R_{22}^2)/2 \\ H = (1/R_{11}^2 + 1/R_{22}^2 - 1/R_{33}^2)/2 \end{cases} \quad (4)$$

For the normal anisotropy materials, $R_{11}$, $R_{22}$ and $R_{33}$ can be determined by Eq.(5).

$$R_{11} = R_{22} = 1, \quad R_{33} = \sqrt{(r+1)/2} \quad (5)$$

where *r* is the normal anisotropy coefficient.

For the as-received tubular material, the normal anisotropy coefficient $r = 1.51$ determined by the uniaxial tension test and the anisotropy coefficients *F*, *G* and *H* are then calculated by Eq. (6).

$$F = G = 1/(2R_{33}^2) = 0.3987, \quad H = 1 - 1/(2R_{33}^2) = 0.6013 \quad (6)$$

By using the associated flow rule as shown in Eq. (7), the relationship between the strain-increment and the stress components can be obtained and formulated in Eq.(8).

$$d\varepsilon_{ij} = d\lambda \frac{\partial f}{\partial \sigma_{ij}} \quad (7)$$

$$\begin{cases} d\varepsilon_1 = d\lambda \left[ 2(G+H)\sigma_1 - 2H\sigma_2 \right] \\ d\varepsilon_2 = d\lambda \left[ 2(H+F)\sigma_2 - 2H\sigma_1) \right] \end{cases} \quad (8)$$

According to Eq.(8), the strain ratio is determined by Eq.(9).

$$\frac{d\varepsilon_1}{d\varepsilon_2} = \frac{(G+H)\sigma_1 - H\sigma_2}{(H+F)\sigma_2 - H\sigma_1} = \frac{(1+R)\sigma_1 - \sigma_2}{(1+R)\sigma_2 - \sigma_1} \quad (9)$$

where *R* is the ratio of the parameters, viz., $G/H = F/H = R$.

For each indentation, $\alpha_i$ can be calculated. For instance, for the orientation a in Fig.1, the following exists:

$$\frac{d\varepsilon_1}{d\varepsilon_2} = \delta \quad (10)$$

By combining Eqs.(9) and (10), the following equation is obtained:

$$\alpha_a = \frac{\sigma_2}{\sigma_1} = \frac{1+R+\delta}{1+\delta+R\delta} \quad (11)$$

Repeating the above operations for all other indenter orientations leads to

$$\alpha_b = \frac{\sigma_2}{\sigma_1} = \frac{1+\delta+R\delta}{1+R+\delta}; \quad \alpha_c = \frac{\sigma_2}{\sigma_1} = \frac{1-R\delta}{1+R+R\delta}; \quad \alpha_d = \frac{\sigma_2}{\sigma_1} = \frac{\delta - R}{R+\delta+R\delta}; \quad \alpha_e = \frac{\sigma_2}{\sigma_1} = \frac{R+\delta+R\delta}{\delta - R};$$

$$\alpha_f = \frac{\sigma_2}{\sigma_1} = \frac{1+R+R\delta}{1-R\delta} \quad (12)$$

- *Evaluation of the anisotropy/asymmetry behaviors of the as-received tubular materials*

Based on the above equations, a load of 200g is applied to conduct the Knoop microhardness

tests. For each direction, the measurements are made at fifteen different positions to have a good statistical average and the indentation spots are carefully chosen to avoid overlapping deformation zones. The surface being tested experiences a high metallographic finish with the small load used. The microscope is used to measure the indentations, which usually has a typical resolution level of 0.2 μm. The hardness is measured using a THV-1MD KHV tester. The detailed measured KHVs are listed in Table 2.

Fig. 6 (a) shows the obvious anisotropy and asymmetry in the locus of KHV, and it can be confirmed that the Knoop hardness data can well represent the anisotropy and tension-compression asymmetry of materials. According to Eqs.(11), (12) and (2), the stress ratio $\alpha_i$ and the converted stress data are calculated, then the plane yield locus of the as-received tubular material is depicted in Fig.6(b). The yield locus can be plotted by a smooth curve connecting the raw KHV point, or by the best fit ellipse method (Fitzgibbon et al. (1999)) and the real coefficient polynomial function. In this research, the measured points are fitted by using a cubic polynomial function presented in Eq. (13). It is noted that, assuming the normal anisotropy coefficient $r=1$, the above equations are converted to **those previous publications reported using Levy–Mises**. Fig.6 (b) shows that, compared with the isotropic yielding, the as-received HSTT presents an obvious distorted yield loci by the two types of Knoop indentation-based methods. Whether the enhanced algorithm by introducing the Hill'48 criterion can describe more reasonably the distorted yielding of the tubular materials will be discussed in Section 4.2.3.

$$f(x,y)=Ax^3+By^3+Cx^2+Dy^2+Exy+Fx+Gy-1 \tag{13}$$

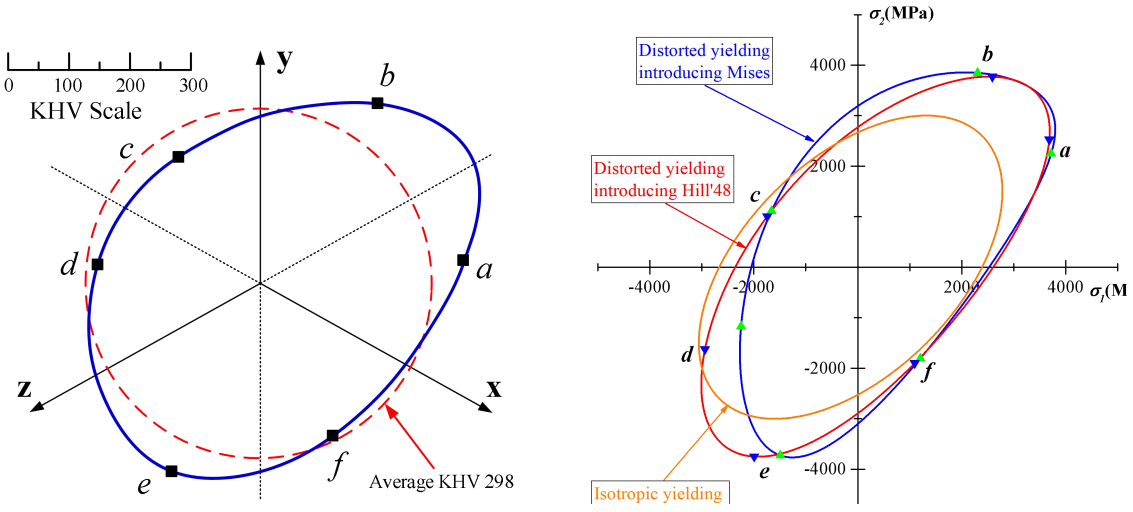


(a) (b)

**Fig.6.** Knoop microhardness based yield locus: a) The locus of KHV in the octahedral plane; b) The locus of yield stress in the plane stress plane

What is the useful of the green “triangle”

**Table 2**. Knoop hardness results.

| *Datum number* | *KHV in different orientations (kg/mm²)* | | | | | |
|---|---|---|---|---|---|---|
| | *a* | *b* | *c* | *d* | *e* | *f* |
| *1* | *329.8* | *370.9* | *252.8* | *288.6* | *339.9* | *276.8* |
| *2* | *346.0* | *365.8* | *243.5* | *282.3* | *326.2* | *274.1* |
| *3* | *339.9* | *320.0* | *255.2* | *286.9* | *326.2* | *261.6* |
| *4* | *337.7* | *327.6* | *238.2* | *267.2* | *347.5* | *270.9* |
| *5* | *339.2* | *321.4* | *245.8* | *266.2* | *316.7* | *241.8* |
| *6* | *316.0* | *318.7* | *239.5* | *295.7* | *339.9* | *248.1* |
| *7* | *301.9* | *349 .0* | *248.1* | *280.7* | *319.4* | *265.7* |
| *8* | *320.0* | *339.2* | *244.0* | *262.6* | *349.0* | *265.2* |
| *9* | *338.5* | *346.0* | *254.7* | *271.9* | *325.5* | *243.5* |
| *10* | *331.2* | *348.3* | *220.5* | *265.7* | *327.6* | *241.3* |
| *11* | *340.7* | *346.0* | *253.8* | *256.2* | *334.1* | *267.2* |
| *12* | *347.5* | *349.8* | *265.2* | *252.8* | *313.4* | *287.5* |
| *13* | *321.4* | *342.9* | *232.2* | *289.8* | *331.2* | *288.6* |
| *14* | *339.2* | *339.9* | *240.4* | *270.4* | *333.3* | *293.3* |
| *15* | *341.4* | *329.1* | *249.0* | *266.7* | *344.4* | *289.2* |
| *Average* | *332.9* | *340.9* | *245.6* | *260.2* | *331.6* | *267.8* |

## *2.3 Uniaxial tension/compression tests of tubular specimens*

As shown in Fig.7 (a), the uniaxial tension/compression tests are conducted for the pieces of tube specimens directly cut from the raw tube. Both the longitudinal and vertical extensometers are used for accurate recording of strain. The velocity is 5 mm/min to ensure quasi-static deformation. Among different heights of the compression specimens, viz., $H$={1.5, 2, 3, 4, 5, 6}mm, the height of 2mm can ensure a stable compression deformation without obvious barreling, distortion and buckling instabilities. The tension/compression stress-strain curves are presented in Fig.7 (b), which indicates an obvious T-C asymmetry.

Similar to the Lankford coefficient $R$-value, contractile strain ratio (CSR) measurements is used to evaluate the anisotropy of the tubular materials (SAE, 2013), which is defined as the ratio of circumferential strain to radial strain for a given tensile strain of **3.5%**. Here, the digital speckle strain measurement method (Yang et al., 2010) is employed to evaluate the *CSR*-value of the HSTT against strain. Fig.7 (b) shows the variation of the *CSR*-value against axial plastic strain.

It is found that *CSR* is not a constant, but decreases and then stabilizes with the increase of the deformation. This indicates the nonnegligible evolution of the anisotropic plasticity of HSTT.

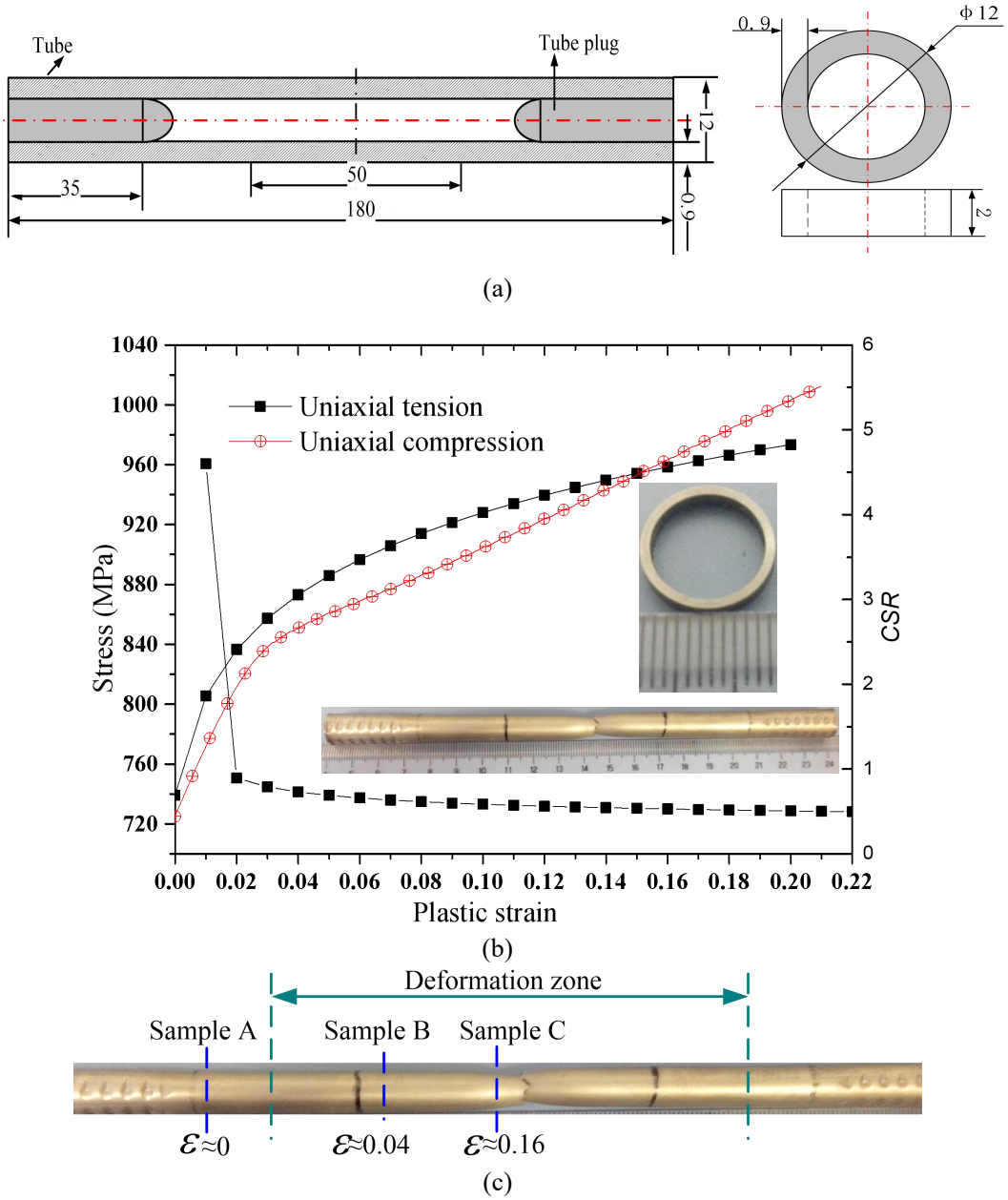


**Fig.7.** Uniaxial tension/compression of tubular specimen along the rolling direction: (a) tubular specimens; (b) stress-strain curves and CSR value; (c) measure locations.

## *2.4 Micro texture and microstructure? evolution identified by EBSD*

The metallographic micro texture of the as-received tubular material and its evolution intension/compression deformation are quantified using SEM-EBSD method. The scanning area of each color map is 50×50μm with a step size of 0.1μm in a MIRA3XMU equipped with an HKL EBSD system. The EBSD data processing procedure is designed using the Channel5 software. From EBSD data, the crystallographic orientation distribution (COD) is determined by using MTEX method (Hielscher and Schaeben, 2008).

It is known that the HSTT is fabricated by multi-pass cold rolling with a large accumulated plastic deformation and incomplete annealing, the internal residual stress thus exists to cause difficulty in sampling for a better Kikuchi pattern. The approaches of grinding, mechanical polishing and electropolishing are used to prepare the EBSD samples, which are thin rings with the height of about 1mm directly cut from the tensioned and compressed tubes by wire cutting. The thin ring is chemically thinned to achieve the final thickness to accommodate the elastic flattening. The cross-section surface normal to the rolling direction of tube is mechanically polished and finally electro-polished using a 10% perchloric acid + 90% glacial acetic acid solution at 50V and 10~20℃ for 60s. As shown in Fig.7(c), for the tension samples, three subsamples of A, B and C are cut from the selected positions with different tensile plastic strains, viz., 0, 0.04 and 0.16; For the uniaxial compression, the cross-section of the compressed sample normal to the compression direction is measured.

Fig. 8 shows the evolution of micro texture of HSTT during tension and compression processes. As shown in Fig. 8(a), the initial texture of the as-received materials (sample A) is characterized by a near radial texture (<0001>//ND); While as shown in Fig. 8 (b) and (c), the c-axes of the HCP crystals gradually reorientate toward the TD direction with the increase of tensile deformation, and finally turn into the tangent texture(<0001>//TD). However, after compression, Fig. 8(d) shows that the c-axes reorientate toward RD and TD directions, and turn into the coexisting states of both the rolling texture(<0001>//RD) and the tangent texture(<0001>//TD), in which the rolling texture intensity is larger than that of the tangent texture. The radial texture disappears finally.

In light of the relationship between the crystallographic orientation and the nature of the activated slip and twinning systems as well as the rationality of Schmid law, both the Schmid factor for slip systems and the volume fraction evolutions of several twinning systems are presented by EBSD as shown in Fig.9. The possible slipping systems and twinning modes are presented, viz., Basal slip {0001}<11-20>, Prismatic (Pr) slip {10-10}<11-20>, First-order Pyramidal (Py<a>) {10-11}<11-20>, Second-order Pyramidal (Py<c+a>), Tensile twinning (Tt){10-12}<10-1-1>, Tensile twinning (Tt) {11-21}<11-2-6>, Compressive twinning (Ct) {11-22}<11-2-3> and Compressive twinning (Ct) {11-11}<-10-1-2> (Bridier et al., 2005).

Fig.9 (a) shows the volume fraction tendencies of grains with hard orientation along with tension deformation. The hard orientation refers the Schmid factor less than 0.25. It is shown that the Basal gliding remains hard status along the tension deformation. While, Pr, Py<a> and Py<c+a> remain softer orientation with the Schmid factor larger than 0.25. Due to the reversible

feature of the gliding, it can be concluded that no matter how the tension or compression is concerned, the primary slip system of HSTT is Pr, Py<a> and Py<c+a>. However, for the twinning activity, its polarity nature requires independent identification in tension and compression. Fig. 9(b) shows that, during tension, the volume fractions of tensile twinning are less than 0.8%, and the (Tt){10-12}<10-1-1> change relatively significantly, thus this twinning can be thought as one of the dominated twinning mechanisms in tension; On the contrary, as shown in Fig. 9(c), it is noted that much more volume fraction of twinning up to 2.6% is observed in the compression. In summary, both the tensile twinning (Tt) $\{10\bar{1}2\}\langle 10\bar{1}\bar{1}\rangle$ and the compressive twinning (Ct){11-22}<11-2-3> can be regarded as the dominant twinning modes in deformation of titanium tubular materials. The identification of these physical mechanisms lays a basis for the VPSC calibration.

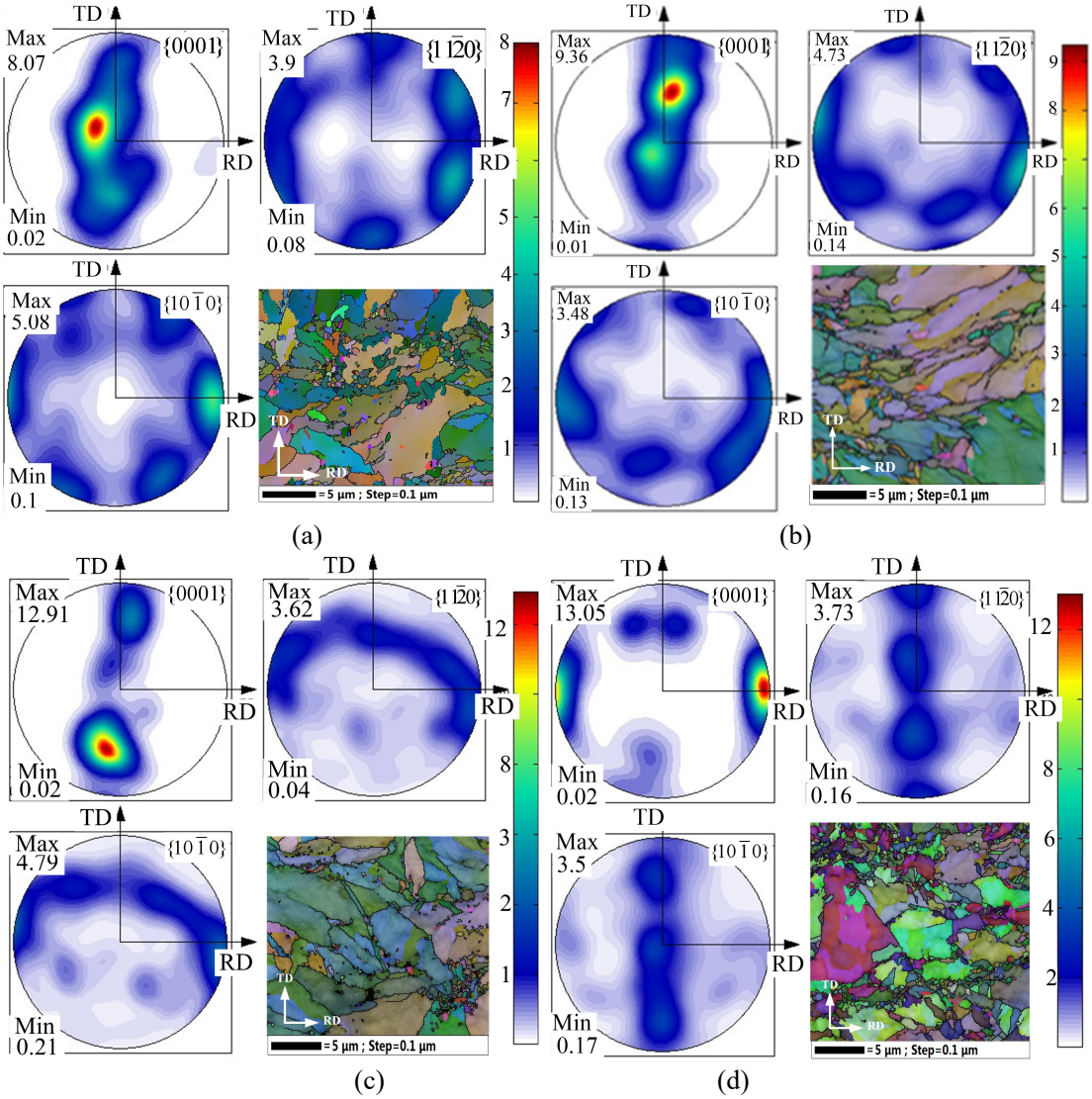


**Fig. 8.** Texture of HSTT in tension and compression deformation: (a) tension sample A; (b) tension sample B; (c) tension sample C; (d) after compression of 50%.

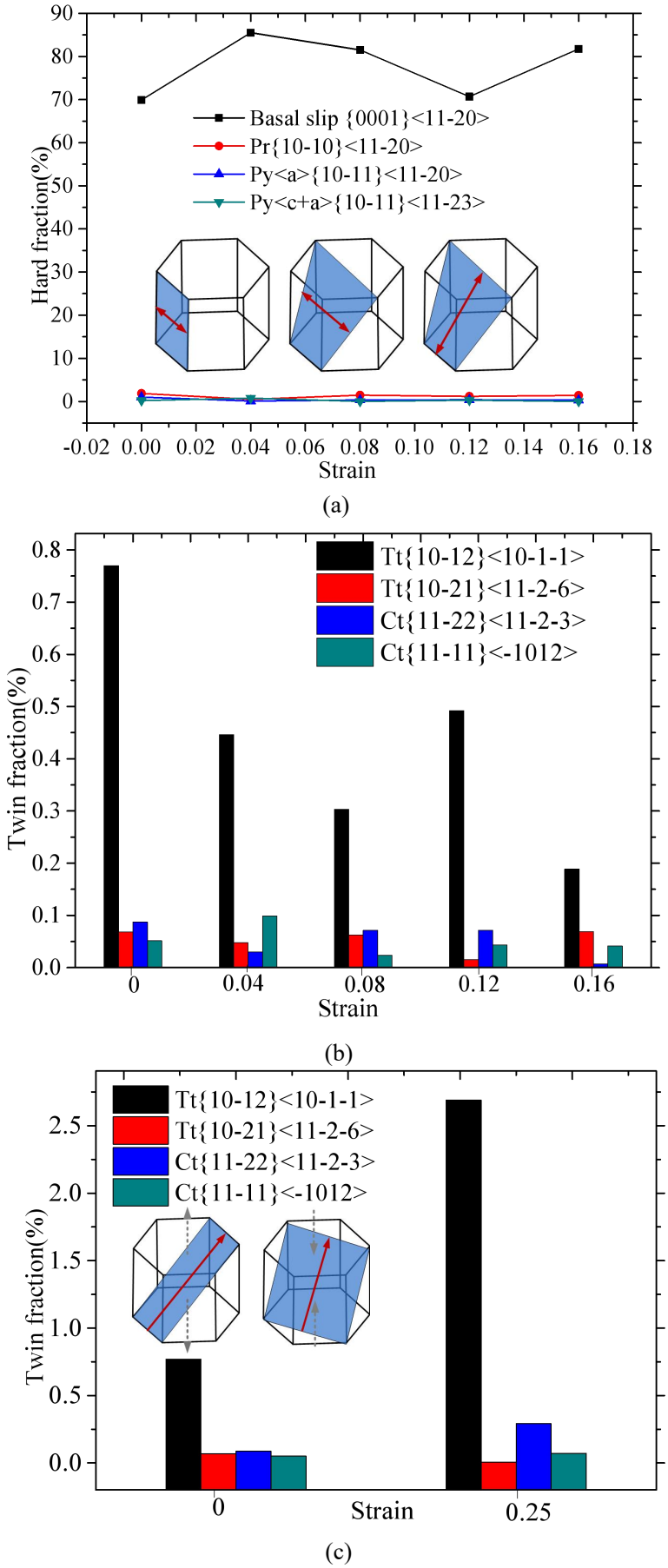


**Fig. 9.** Evolution of slipping and twinning: (a) volume fraction of grains with hard orientation in tension;

(b) twin volume fraction in tension; (c) twin volume fraction in compression.

# 3. VPSC-based crystal plasticity modeling

## *3.1 Basic assumptions and governing equations*

The VPSC modeling is based on the assumption that each grain can be treated as an anisotropic visco-plastic ellipsoidal inclusion (Eshelby, 1957) embedded and interacted with a homogeneous visco-plastic effective medium (MEM) that represents the polycrystalline aggregate with the average constitutive behavior. The inclusion and medium have fully anisotropic properties. Deformation is based on crystal plasticity mechanisms, and both the slip and twinning activations are considered (Tomé et al., 2012). Since the rolled materials are dense enough, the non-reversible slip modes are not considered. The viscoplastic constitutive behavior at local level in a given grain is described by the non-linear rate-sensitivity equation below:

$$\varepsilon_{ij} = \sum_s m_{ij}^s \gamma^s = \gamma_0 \sum_s m_{ij}^s \left(\frac{m_{kl}^s \sigma_{kl}}{\tau_0^s}\right)^n \tag{14}$$

where $\tau^s$ is the critical resolved shear stress (CRSS) on slip or twinning system *s*, $m_{ij}^s = (n_i^s b_j^s + b_j^s n_i^s)/2$ is the Schmid tensor associated with slip or twinning, $n^s$ and $b^s$ are the normal and Burgers vectors in the slip or twinning system, $\varepsilon_{ij}$ and $\sigma_{kl}$ are the deviatoric strain rate and stress, $\gamma^s$ is the local shear rate on system *s*, $\gamma_0$ is a normalization factor and *n* is rate-sensitivity exponent.

Such self-consistent polycrystal formalism needs an interaction equation that linearly relates the stress and strain rate of the effective medium. The condition that the averages of stress and strain rate over all the grains have to be consistent with the equivalent macroscopic magnitudes, making the self-consistent resolution of the problem and ensuring both the strain compatibility and stress equilibrium (Lebensohn et al., 1996, Lebensohn and Canova, 1997). In addition, Fig.10 shows the detailed calculation procedure of the VPSC-based crystal plasticity modeling. In the following, only the hardening formulas and the twinning model are briefly presented.

Among several hardening models such as Mechanical Threshold Stress (MTS) hardening and dislocation density models, an extended Voce hardening law, as shown in Eq. (15), is used to describe the evolution of the threshold stress with accumulated shear strain in each grain for individual deformation system including slip and twinning systems.

$$\tau^s = \tau_0^s + \left(\tau_1^s + \theta_1^s \Gamma\right)\left[1 - \exp\left(-\theta_0^s \Gamma \Big/ \tau_1^s\right)\right] \tag{15}$$

where $\tau^s$ is the instantaneous CRSS, $\Gamma = \sum_s \Delta\gamma^s$ is the accumulated shear in the grain, $\tau_0^s$ and $\tau_0^s + \tau_1^s$ are the initial CRSS and the final back-extrapolated CRSS, $\theta_0^s$ and $\theta_1^s$ are the initial hardening rate and the asymptotic hardening rate, respectively.

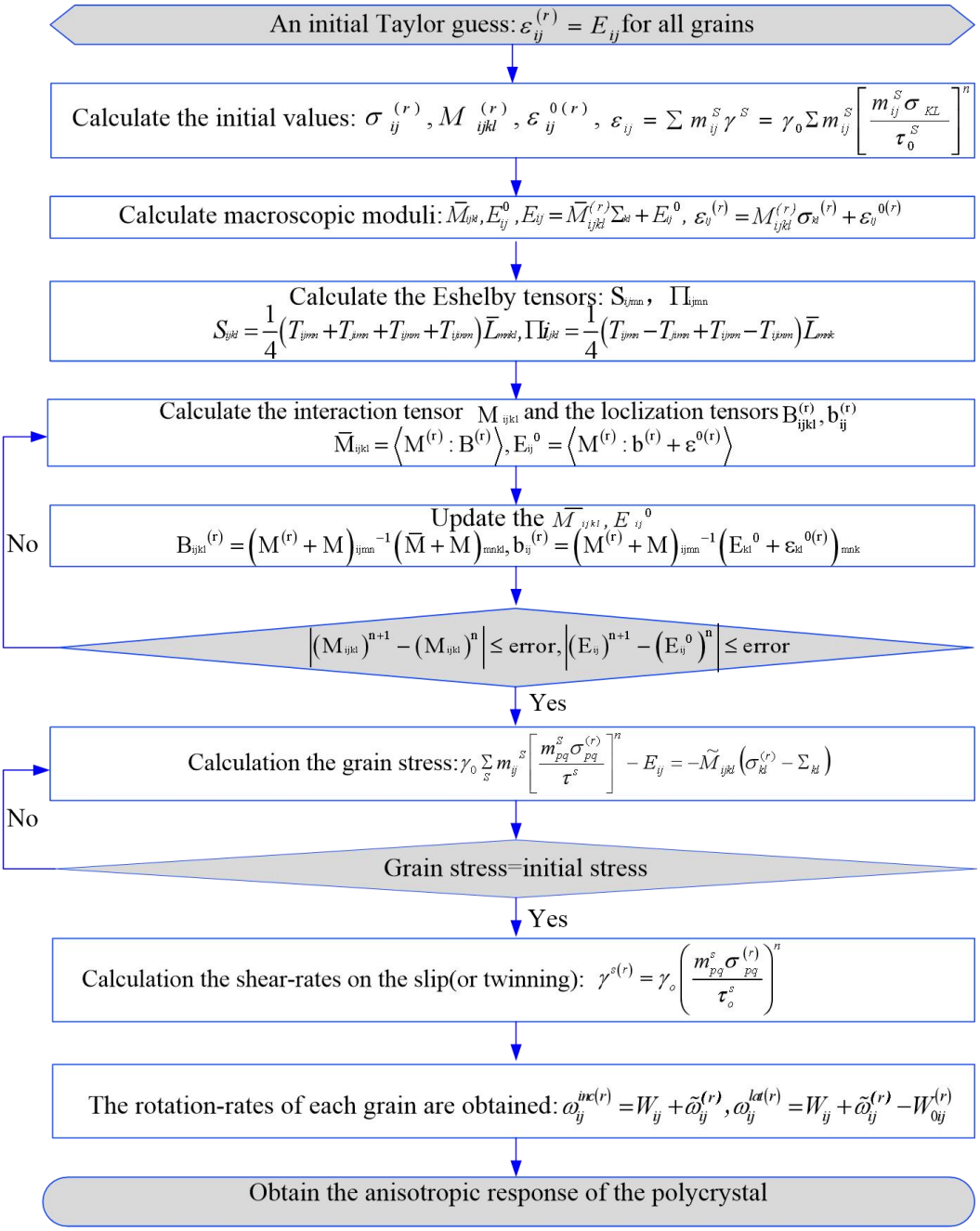


Note: $m_{ij}^S, \gamma S$ —Symmetric schmid tensor and shear-rate associated with slip system(S),respectivly
$S_{IJKL}\Pi_{IJKL}$—Symmetric and skew-symmetric Eshelby tensor,respectivly
$M_{IJKL}^{(r)}\varepsilon_{ij}^{0(r)}$ —The viscoplastic compliance an back-extrapolated of grain(r),respectivly
$T_{ijkl}$ —Green interaction tensor; $n$ —Rate-sensitivity exponent; $\gamma_0$ —Normalization factor
$\omega_{ij}^{inc(r)}, \omega_{ij}^{lat(r)}$—The rotation-rates of the inclusion and the lattice,respectivly

**Fig.10.** Calculation procedures of VPSC-based crystal plasticity modeling.

The model allows for 'self' and 'latent' hardening by introducing coupling coefficient $h^{ss'}$ empirically accounting for the obstacles that new dislocations $s'$ represent the propagation of system $s$:

$$\Delta\tau^s = \frac{d\tau^s}{d\Gamma}\sum h^{ss'}\Delta\gamma^{s'} \tag{16}$$

where $\Delta\tau^s$ is the increase of the CRSS of a slip system due to shear activity $\Delta\gamma^{s'}$.

Though twinning is assumed to be associated with CRSS in the twinning plane along the twinning direction, it differs from the reversible gliding in its direction and is modeled by allowing activation only if the resolved shear stress is positive along the Burgers vector of the twinning. The occurrence of twinning (lamellar morphology) not only significantly changes the aggregate texture by reorienting the twinned volumes relative to the surrounding matrix, but also acts as an effective barrier for the activation and propagation of dislocations by easier slipping or other twin lamellae. As shown in Eq. (16), this barrier effect on slip and twinning systems can be empirically described by assigning high value to the coupling coefficient $h^{ss'}$.

The contribution of twinning to the texture development can be modeled by the predominant twin reorientation scheme (PTR) and the volume fraction transfer scheme (VFT) (Tomé et al., 1991). The VFT scheme is used to describe the reorientation due to twinning from a numerical point of view. For the PTR scheme, within each grain *g*, both the shear strain $\gamma^{t,g}$ contributed by each twin system *t* and the associated volume fraction $V^{t,g} = \gamma^{t,g} / S^t$ ( $S^t$ is the characteristic twin shear) are recorded. The sum over all the twin systems of a certain mode (eg., tensile twins or compressive twins) and over all the grains represents the accumulated twin fraction $V^{acc,mode}$ in the aggregate for the particular twin mode:

$$V^{acc,mode} = \sum_g \sum_t \frac{\gamma^{t,g}}{S^t} \tag{17}$$

Since it is not numerically feasible nor physically justifiable to regard each twinned fraction as an independent new grain, the PTR scheme adopts a statistical approach, viz., at each increment, some grains are fully reoriented by twinning provided that the accumulated twin fraction is larger than the so-called threshold volume fraction $V^{th}$, as shown in Eq.(18).

$$V^{th} = A^{th1} + A^{th2}\frac{V^{eff}}{V^{acc}} \tag{18}$$

$V^{eff}$ is the effective twinned fraction, which is the volume fraction represented by these fully reoriented grains for each of the twin modes. The process is repeated until either all grains are randomly checked or until the effective twin volume exceeds the accumulated twin volume. It is noted that: 1) only the historically most active twin system in each grain is considered for reorienting the whole grain by twinning; 2) the twinning fraction is kept consistent with the shear activity that the twins contribute to deformation. This algorithm prevents grain reorientation by twinning until a threshold value $V^{th1}$ is accumulated in any given system (typically 10-25% of grain volume) and rapidly increases to the threshold to a value around $A^{th1} + A^{th2}$ (typically 50-60% of grain volume). The twin reoriented grains undergo a second reorientation by twinning.

### *3.2 Establishment of boundary conditions for instantaneous deformation*

The VPSC-based crystal plasticity computation needs two basic inputs, viz., the initial crystallographic textures and loading/strain boundary conditions (overall velocity gradient components or overall stress components).

The texture input can be either directly measured by SEM-EBSD probing or parametrically generated by the statistical method. It is noted that the as-received material is the stress relieved titanium tube with a large number of cold working produced grains. Due to the high degree of deformation, most of the misorientation distributions are low angle boundaries in the EBSD scanned areas, which leads to many different crystal orientations in the same grain. Therefore, every scanning outputs a crystal orientation, viz., three Euler angles, and the number of the scanning points in the EBSD result is 28603. For the as-received material, a total of 28603 crystal orientations are directly used in VPSC computation.

For the boundary conditions, the velocity gradient components (strain rate and spin), stress components or a combination of strain-rate and stress components are imposed to the aggregates. In this research, the velocity tensor $\dot{L}$ is used to specify which deformation components should be enforced. There are two ways for assigning the velocity gradient. The first one is to fix the velocity gradient during each incremental deformation; while the latter is to impose the variable velocity gradient at each iteration step, which reflects the instantaneous deformation history. As shown in Table 3, for simple loading conditions such as uniaxial tension and compression, the fixed velocity gradient can be analytically calculated and is enough to represent the monotonic deformation history. For most metal forming processes, however, the deformation is non-proportional and non-steady, the variable velocity gradient should be feasible. The explicit

3D-FE simulation combined with Abaqus/Vumat subroutine is used to obtain the deformation gradient, and thus the variable velocity gradients can further be calculated by using Eq. (19). The advantage of this approach is accurately accounting for the instantaneous deformation history.

$$\left[L^t\right]=\left\{\left[F^{t+\Delta t}\right]-\left[F^t\right]\right\}/\left\{\left[F^{t+\Delta t}\right]\Delta T\right\} \tag{19}$$

where $L^t$ is the velocity gradient for time *t*, $F^t$ and $F^{t+\Delta t}$ are the deformation gradients for time $t$ and $t+\Delta t$, respectively.

**Table 3.** Boundary conditions imposed on the polycrystals for the VPSC simulation.

| Test | RD tension/compression | TD tension/compression | ND tension/compression |
|---|---|---|---|
| Velocity gradient tensor | $\begin{bmatrix} \dot{\varepsilon} & 0 & 0 \\ 0 & -\dot{\varepsilon}/2 & 0 \\ 0 & 0 & -\dot{\varepsilon}/2 \end{bmatrix}$ | $\begin{bmatrix} -\dot{\varepsilon}/2 & 0 & 0 \\ 0 & \dot{\varepsilon} & 0 \\ 0 & 0 & -\dot{\varepsilon}/2 \end{bmatrix}$ | $\begin{bmatrix} -\dot{\varepsilon}/2 & 0 & 0 \\ 0 & -\dot{\varepsilon}/2 & 0 \\ 0 & 0 & \dot{\varepsilon} \end{bmatrix}$ |

Note: the strain rate $\dot{\varepsilon}$ is positive for tension and negative for compression, respectively.

### *3.3 Compression-based orthogonal inverse method for parameters calibration*

One of the most difficult tasks in crystal plasticity modeling is to determine the accurate parameter values for generating the best simulation results, whilst still being realistic and well constrained. There are two kinds of parameters for VPSC, viz., the numerical implementation related parameters and the crystal plasticity related ones. Since the values of the former parameters are generally defaulted, the latter ones are the focus in this section. According to the used Voce hardening and latent hardening, a total nine types of parameters should be calibrated, viz., Voce hardening related parameters $\tau_0^s$, $\tau_1^s$, $\theta_0^s$, $\theta_1^s$; and latent hardening related parameters $h_s^{Pr}$, $h_s^{Py<a>}$, $h_s^{Py<c+a>}$, $h_s^{Tt}$, $h_s^{Ct}$. In addition, for the two twinning mechanisms, three kinds of PTR scheme related parameters, viz., twin shear *S*, $A^{th1}$ and $A^{th2}$, should be calibrated. Both $S^{Tt}$ and $S^{Ct}$ are assigned as 0.174 and 0.219, respectively; $A^{th1}$ and $A^{th2}$ are given by 0.2 and 0.5, respectively (Eshelby, 1957). The rate-sensitivity exponent *n* is 25.

As identified in Section 2, three gliding systems (Pr, Py<a> and Py<c+a>), two twinning modes (tensile twinning (Tt) $\{10\bar{1}2\}<10\bar{1}\bar{1}>$ and compressive twinning (Ct) $\{11\bar{2}2\}<11\bar{2}\bar{3}>$) are the dominant mechanisms for HSTT, and there are a total of 45 parameters for VPSC-based crystal plasticity modeling of HSTT. Due to a large number of fitting parameters, testing the validity of all the combinations of parameters against the experimental data is impractical. A possible way is to use an optimization method to automatically find the best set of parameter

combination. However, such a method has its own computational requirements and complications (e.g. avoiding false minimal) and is not available at present. Here, the parameter set is determined through an orthogonal virtual experiment fitting of the experimental stress-strain curve. Meanwhile, since the number of the involved mechanisms for accommodating the compression deformation is more than that for tensile deformation, only the experimental data of compression is used for parameter calibration. The axial tensile tests and a more complex process, viz., mandrel bending, are used for validation of the established VPSC-based crystal plasticity modeling from the aspects of both stress-strain curves and texture evolutions. The strain rate $\dot{\varepsilon}$ is 0.005 $s^{-1}$ for calculation of the static velocity gradient of tension and compression, and the variable velocity gradients are obtained for mandrel bending.

The initial values and selection ranges of the above hardening parameters for each deformation mechanisms ( $\tau_0$ , $\theta_0$ , $\tau_1$ , $\theta_1$ , $h_s^{Pr}$ , $h_s^{Py<a>}$ , $h_s^{py<c+a>}$ , $h_s^{Tt}$ , $h_s^{Ct}$ ) are selected based on a statistical analysis of the results previously reported (Eshelby,1957; Lebensohn and Canova,1997; Fundenberger et al.,1997; Balasubramanian and Anand,2002; Salem et al.,2005; Yapici et al., 2006; Wu et al.,2007; Gurao et al.,2011; Abdolvand and Daymond,2012). The results are as follows:

- For $\tau_0$ , $\tau_0^{Pr}$ is 15~120MPa, $\tau_0^{Py<a>} / \tau_0^{Pr}$ is about 10; $\tau_0^{Py<c+a>}$ is 250~450MPa, $\tau_0^{Py<c+a>} / \tau_0^{Pr}$ is about 4; $\tau_0^{Tt}$ is 50~250MPa, $\tau_0^{Tt} / \tau_0^{Pr}$ is about 2; $\tau_0^{Ct} / \tau_0^{Pr}$ is about 4;
- For $\tau_1$ , $\tau_1^{Pr}$ is 30~70MPa; $\tau_1^{Py<a>}$ is 0-30MPa; $\tau_1^{Py<c+a>}$ is 190-270MPa; $\tau_1^{Tt}$ is 0~35MPa or 200~220MPa; $\tau_1^{Ct}$ is 0-30;
- For $\theta_0$ , $\theta_0^{Pr}$ is 100~2000; $\theta_0^{Py<a>}$ is about 1000; $\theta_0^{Py<c+a>}$ is 200~3000; $\theta_0^{Tt}$ 50~100;
- For $\theta_1$, $\theta_1^{Pr}$ is 0~1, $\theta_1^{Py<a>}$ is 178-450; $\theta_1^{Py<c+a>}$ is about zero; $\theta_1^{Tt}$ is 10~75; $\theta_1^{Ct}$ is 178~450;
- The coupling coefficients $h^{ss'}$ between slip and slip are set to one, and the slip-twinning coefficient and the twinning-twinning one are set to 5 and 10, respectively.

### *3.4 Evaluation of the established VPSC crystal plasticity model*

Table 4 shows the finally obtained parameters by the compression-based orthogonal inverse method. Regarding the macroscopic stress-strain curves and the micro texture evolution in uniaxial tension/compression tests and mandrel bending with spatial inhomogeneous deformation, the calibrated VPSC crystal plasticity model is thoroughly validated from different

aspects.

**Table 4.** Final parameters for VPSC modeling of HSTT.

| | $\tau_0$ | $\tau_1$ | $\theta_0$ | $\theta_1$ | $h_s^{*,pr}$ | $h_s^{*,B}$ | $h_s^{py<c+a>}$ | $h_s^{*,Tt}$ | $h_s^{*,Ct}$ |
|---|---|---|---|---|---|---|---|---|---|
| Pr | 235 | 80 | 2485 | 50 | 1 | 1 | 1 | 5 | 3 |
| Py<a> | 620 | 95 | 500 | 100 | 1 | 1 | 1 | 5 | 5 |
| Py<c+a> | 565 | 45 | 800 | 50 | 1 | 1 | 1 | 5 | 5 |
| Tt | 570 | 0 | 2000 | 50 | 5 | 5 | 5 | 1 | 10 |
| Ct | 545 | 0 | 2000 | 50 | 5 | 5 | 5 | 10 | 10 |

Note: The latent hardening parameters have no unite. The unit for all other parameters is MPa.

As shown in Fig.11, the predicted stress-strain curves in uniaxial compression agree well with the experimental ones. In particular, with the same set of parameters calibrated by the compression-based orthogonal inverse method, there is a very good fitting to the uniaxial tension experiments in terms of the stress-strain curve.

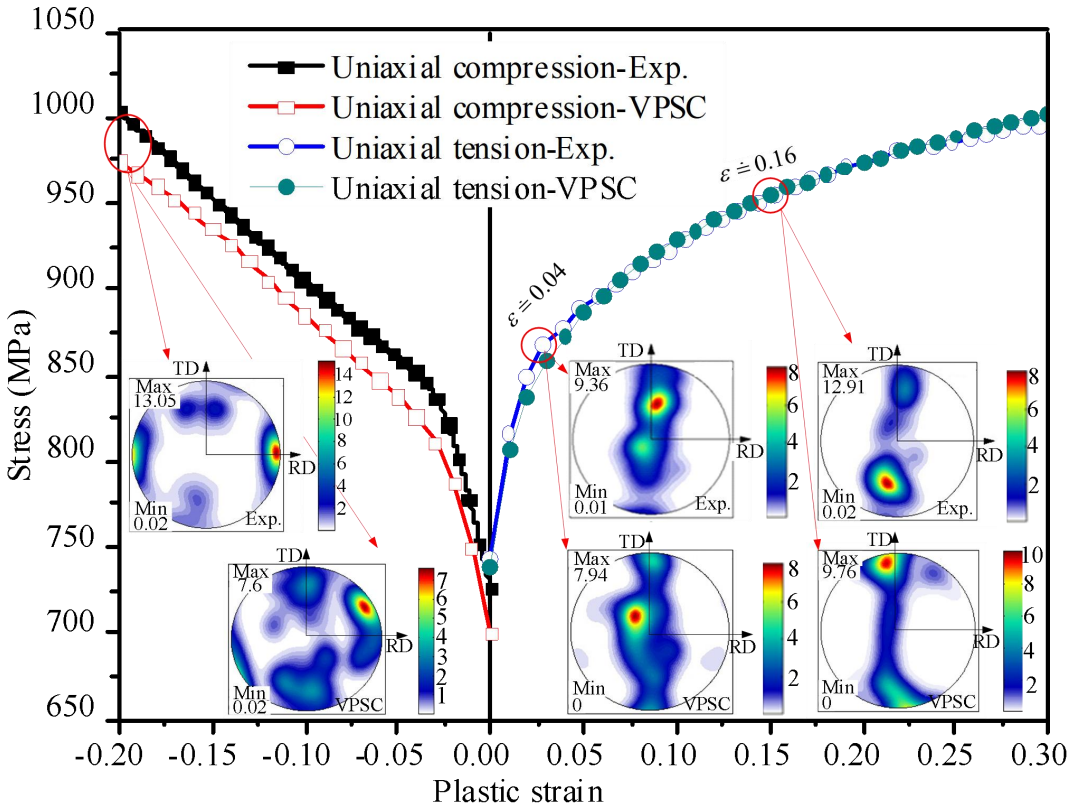


**Fig.11.** Comparison of the experimental and prediction results of {0001} pole figures for uniaxial tension/compression tests.

Simultaneously, by comparison of the texture evolution between the predictions and the experimental results, it can be seen that, despite the discrepancy in texture density to some extent, the key features of texture reorientation during uniaxial tension and compression are accurately captured. That is, with the increase of uniaxial tensile deformation, the c-axes of the HCP crystals gradually reorientate toward the TD direction, then the initial texture of a near radial texture (<0001>//ND) gradually turns into the tangent texture (<0001>//TD ); After

compression, Fig.11 shows that the c-axes reorientate toward RD and TD directions, and turn into the coexisting states of both the rolling texture (<0001>//RD) and the tangent texture (<0001>//TD), in which the rolling texture intensity is larger than that of the tangent texture. The radial texture disappears finally.

The reason why the certain discrepancy exists is due to the following causes:

1) Unlike the macroscopic stress-strain curve, the texture distribution is a microstructure feature. The inhomogeneous deformation during uniaxial tension and compression may affect the characterizing accuracy of the micro textures. As shown in Fig. 7(c), for the tension samples, three subsamples of A, B and C are cut from the selected positions with an approximate tensile plastic strain of 0, 0.04 and 0.16, respectively. For the uniaxial compression, the middle cross-section of the compressed sample normal to the compression direction is measured. Though the height of 2mm can ensure a relatively stable compression deformation, a slight barreling still exists.

2) The assumptions made in the VPSC crystal plasticity model surely result in the discrepancy between the predicted textures and the experimental ones. By EBSD analysis in this study, the VPSC crystal plasticity model only considers five main deformation mechanisms, viz., prismatic slip (Pr), pyramidal slip (Py<a>), pyramidal slip (Py<c+a>),tensile twinning (Tt) and the compressive twinning (Ct). Other deformation mechanisms are ignored. In additional, the morphology of the as-received high strength titanium tube is near alpha materials, which is characterized by a large number of cold working produced alpha grains with minor beta phase spread out at grain boundaries. In VPSC-based model, only the alpha phase is considered and the initial grain shape is assumed to be uniformly distributed. Furthermore, the governing equations in VPSC crystal plasticity mode such as the hardening law and twinning rule are established in an empirical way.

To further illustrate the validity of the calibrated VPSC crystal plasticity model, taking the mandrel bending of HSTT as a typical forming case subjected to complex 3D loading of tension and compression, as shown in Fig. 12(a), the comparison of the VPSC predictions with the experimental results is conducted. Upon bending, there occur 3D tensile stress states and 3D compressive stress states at the extrados and intrados of tube simultaneously. Both the tension strain and compression strain at the extrados and intrados of tube are larger than those in uniaxial tension and compression. It can be seen that the stress states in mandrel bending are much complex than those in uniaxial tension and uniaxial compression. In the VPSC-based computation of mandrel bending, the variable velocity gradient throughout the whole bending process is assigned into the VPSC-based crystal plasticity models. In mandrel bending

experiment, the bending radius is 1.5 times the tube diameter, the bending angle is 90° for the designed forming angle of 90° , and the bending velocity is 1° /s . The detailed description of the 3D-FE models of the mandrel bending is given in literature (Li et al., 2012). Using the combination of the VPSC model and Explicit 3D-FE model, the texture evolution along tube bending is captured, as shown in Fig. 12 (b).

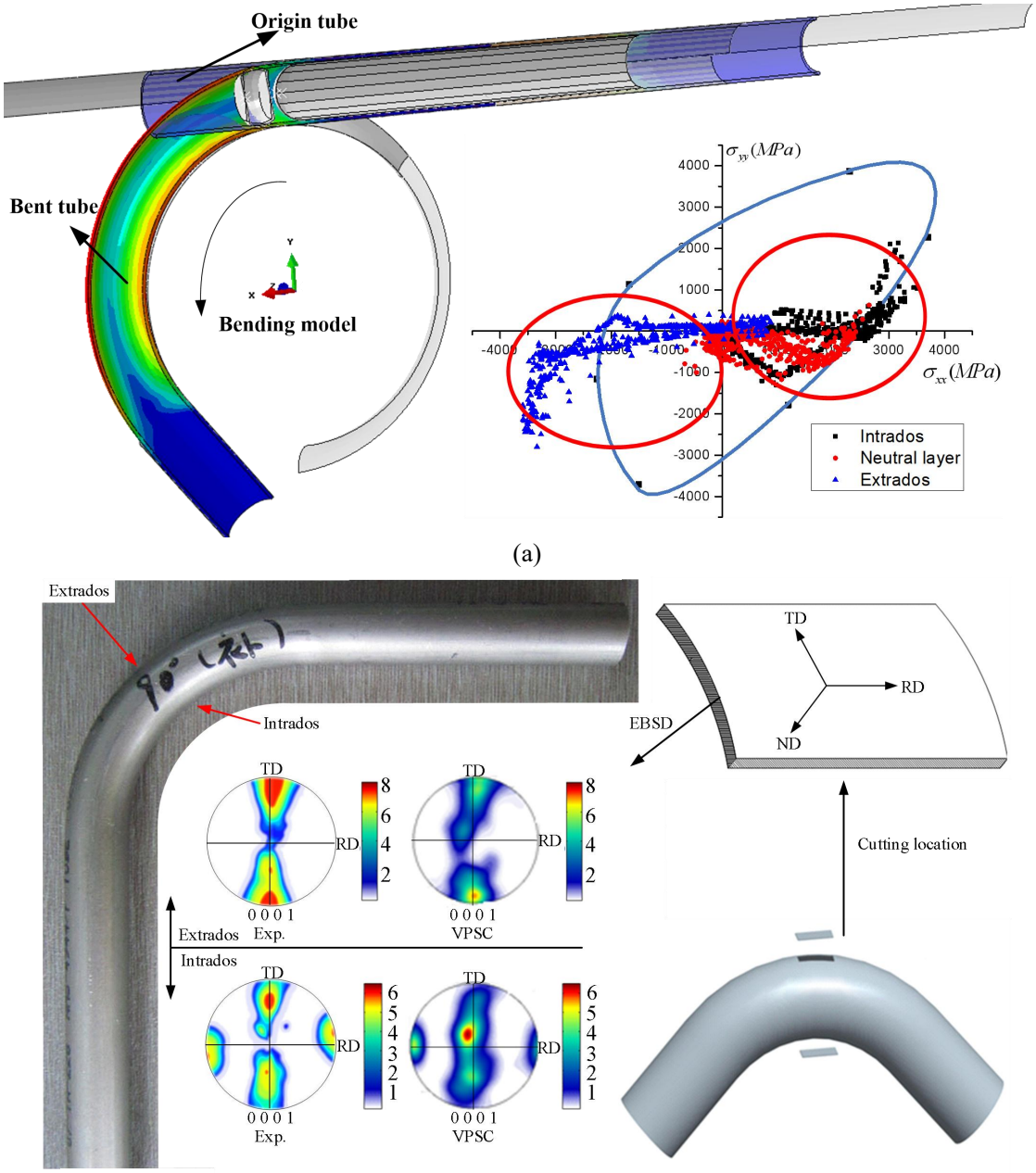


**Fig. 12.** Comparison of the experimental results and the prediction ones of mandrel bending: (a) schematic of bending under non-uniform tension and compression; (b) {0001} pole figures and measuring locations.

As shown in Fig. 12(b), the features of the micro textures during tube bending are accurately predicted. Except for the minor difference in intensity, the simulated results are consistent with the experimental ones and can represent the deformation characteristics, viz., the c-axes of grain

turn toward TD direction at the extrados of tube, and the c-axes of grain reorientate toward RD and TD directions at the intrados of tubes, as shown in Fig. 12(b). It is thus sure that the VPSC crystal plasticity model can work correctly and its calibration is correct. Accurate prediction of the mechanical response and texture evolution indicates that the predicted relative activities of the slip and twin modes contributing to plastic deformation are reasonable.

## 4. Results and discussions

### *4.1 Computation matrix*

By using the VPSC-based virtual experiments with the calibrated crystal parameters, the plastic deformation of titanium tubular materials under the arbitrary loading conditions can be identified and elucidated. A computation procedure of 6 × 6 matrix is given, which is used to represent the tubes with six typical initial textures and under six fundamental loadings.

As shown in Fig.13, a total of six types of initial textures are experimentally or mathematically designed, viz., as-received , bimodal, random, radial, tangential texture and rolling textures. In the VPSC model, each orientation is defined by three Euler angles ( $0 \le \phi_1 \le 2\pi$ , $0 \le \Phi \le \pi$ , $0 \le \phi_2 \le 2\pi$ ) and the associated volume fraction. For the as-received and bimodal textures, we directly considered the total 28603 and 27020 crystal orientations in VPSC-based computation, and for the other initial textures, 2000 crystal orientations are considered. As shown in Fig.14, the computation accuracy can be ensured given enough crystal orientations being considered in the modeling. The methods to obtain the texture of the latter three modes are presented. To obtain the radial texture, the first step is to make $\phi_2$ be an constant, such as $\varphi_2 = 5°, 15°, 25°, 35°, 45°, 55°$ . According to the number of grains needed, $\phi_1$ varies from $0°$ to $360°$ . Since the basal pole may tilt about $\pm 15°$ to $\pm 30°$ from the normal direction towards the rolling and tangential directions, and $\Phi$ may vary from $0°$ to $30°$ . Following this procedure, the radial texture including 2000 discrete orientations is generated. To obtain the tangential and rolling texture, the radial texture may be rotated with $90°$ rigidly around the rolling direction and tangential direction using the rotation matrix as shown in Eq.(20), respectively. The crystal orientation feature of the bimodal texture is its c-axial shifting from radial direction to tangential one with 20°~30°. Finally, the six typical tubular textures including 2000 discrete orientations representing the initial texture are obtained.

$$R_1 = \begin{bmatrix} 1 & 0 & 0 \\ 0 & 0 & -1 \\ 0 & 1 & 0 \end{bmatrix} \text{ and } R_2 = \begin{bmatrix} 0 & 0 & -1 \\ 0 & 1 & 0 \\ 1 & 0 & 0 \end{bmatrix} \tag{20}$$

where, matrix $R_1$ is the rotation matrix around rolling direction and matrix $R_2$ is around tangential direction.

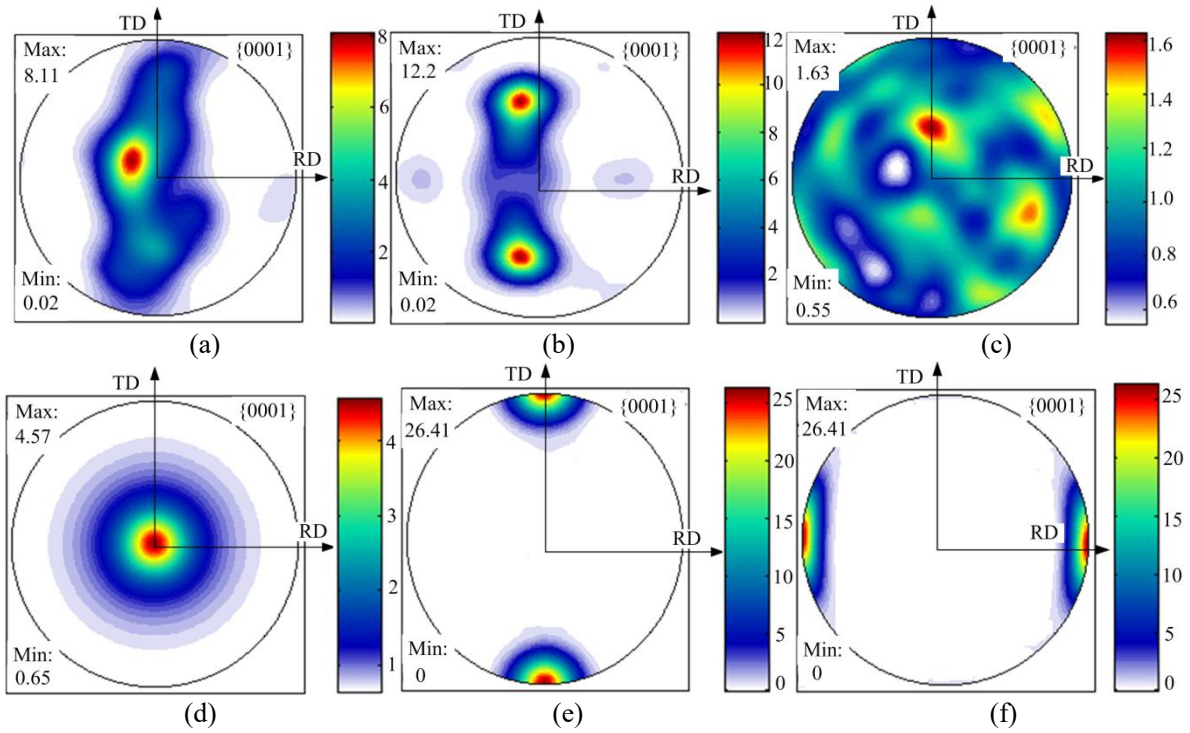


**Fig.13.** Six typical initial textures of the VPSC model: (a) as-received texture; (b) bimodal texture; (c) random texture; (d) radial texture; (e) tangential texture; and (f) rolling texture.

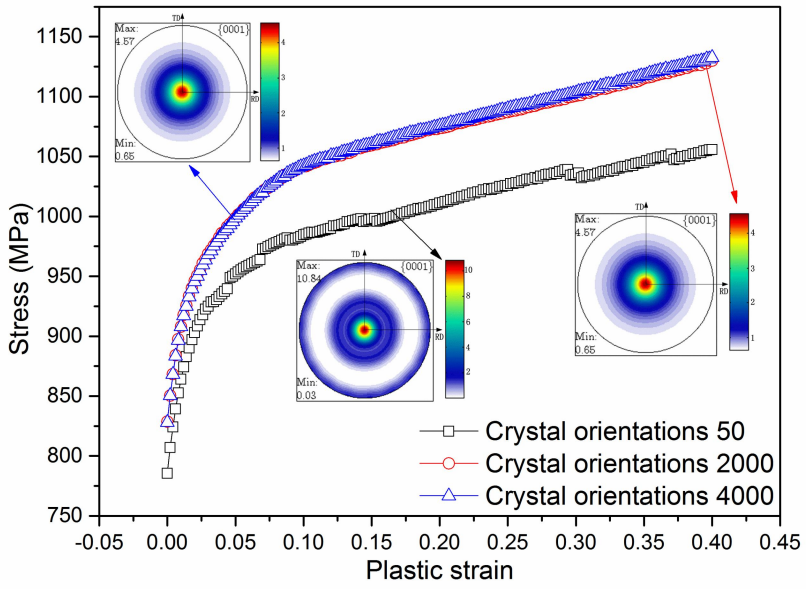


**Fig.14** True stress-strain curves of the radial texture with different orientations.

As shown in Fig.1, six fundamental loading conditions include uniaxial tension/compression along RD direction (marked as *A* and *G*), uniaxial tension/compression along TD direction (marked as *E* and *K*), and the equal biaxial tension and compression in RD-TD plane (marked as

*C* and *I*). For the biaxial tension or biaxial compression loading, as shown in Eq. (21) in the following, the stress states at yielding can be equivalently transformed to the ones under uniaxial

$$\sigma_y = \begin{bmatrix} \pm\sigma & 0 & 0 \\ 0 & \pm\sigma & 0 \\ 0 & 0 & 0 \end{bmatrix} + \begin{bmatrix} \mp\sigma & 0 & 0 \\ 0 & \mp\sigma & 0 \\ 0 & 0 & \mp\sigma \end{bmatrix} = \begin{bmatrix} 0 & 0 & 0 \\ 0 & 0 & 0 \\ 0 & 0 & \mp\sigma \end{bmatrix} \tag{21}$$

compression or uniaxial tension along ND direction, respectively. This equivalence is based on the assumption of hydrostatic pressure insensitivity of yielding for densified matters, which has been verified by several experiments (Barlat et al., 2003; Nixon et al., 2010; Khan and Yu, 2012). Thus, all the six loading conditions can be simplified as the uniaxial deformation and described by the static velocity gradients.

## *4.2 Distorted plastic deformation behaviors*

### *4.2.1 Anisotropic and asymmetry in flow stress*

Fig. 15 shows the true stress-strain curves of the HSTT with different initial textures under different loading conditions. It is found that the strain hardening behaviors for the six initial textures differ greatly. Except for the random texture, there occur remarkable anisotropic behaviors both in tension and compression loading conditions for other five initial textures, and another anomaly for HSTT is the significant T-C asymmetry.

Fig. 15(a) shows that, for the as-received texture, whether in tension or compression state, the flow stress along the ND (with most c-axes), TD (with a little c-axes) and RD (with nearly no c-axes) is the highest, intermediate and lowest, respectively. The HSTT with the as-received texture shows the significant anisotropy in both tension and compression. Meanwhile, the significant T-C asymmetry in the flow stress is observed. For instance, the yield stress in compression along RD is about 684.7 MPa, while it is 744 MPa in tension along RD. The T-C asymmetry is higher along ND than the ones along TD and RD, viz., the strength difference along ND-tension and ND-compression is the most significant.

As shown in Fig. 15(b), for the bimodal texture, more pronounced anisotropic and asymmetric behaviors are observed compared with those of the as-received texture samples. The flow stress in most directions is greater than those in the as-received tubular materials. The flow stress in ND-tension is greater than those in other loading conditions. The highest T-C asymmetry is found in ND direction for bimodal texture. It is also noted that different increasing tendencies occur in tension or compression, viz., the **concaved** up strain hardening responses with the positive strain hardening slope, while the **convexed** up hardening responses with the negative

strain hardening slope. More remarkable concaved and convexed increase of strain hardening is observed for either tension or compression deformation along ND and TD.

As for the samples with random texture, as shown in Fig. 15(c), the yielding behaviors, viz., isotropy and symmetry, coincide in all directions no matter in tension or compression at the early deformation stage. The minor anisotropy and T-C asymmetry occur when the strain is about 20% due to the formation of textures. For the radial texture samples, as shown in Fig. 15(d), the anisotropy and T-C asymmetry are the highest with the loading direction along ND direction, viz., the loading direction parallel with the c-axis. In contrast to that along ND direction, the mechanical responses of tension/compression in RD/TD directions are almost the same due to the cylindrical symmetry of the HCP structure. As shown in Fig. 15 (e) and (f) and compared with the radial texture sample, both the tangential and rolling texture samples show the similar anisotropy and T-C asymmetry. It can thus be summarized that the anisotropy and the T-C asymmetry are highest when the loading direction is inclined to the c-axes.

The above results show that, for each initial texture, the anisotropy and T-C asymmetry are strongly dependent on the predominant orientation of the c-axes with respect to the loading directions. A similar result has also been reported by Agnew et al. (2005). Since there are positive and negative strain hardening behaviors for several initial textures, the widely used exponent hardening law such as $\sigma = K\left(\varepsilon_0 + \varepsilon\right)^n$ cannot be used for calibrating the strain hardening characteristics. For instance, the strain hardening exponent should be negative for bimodal texture and radial texture by using the above exponent hardening equation.

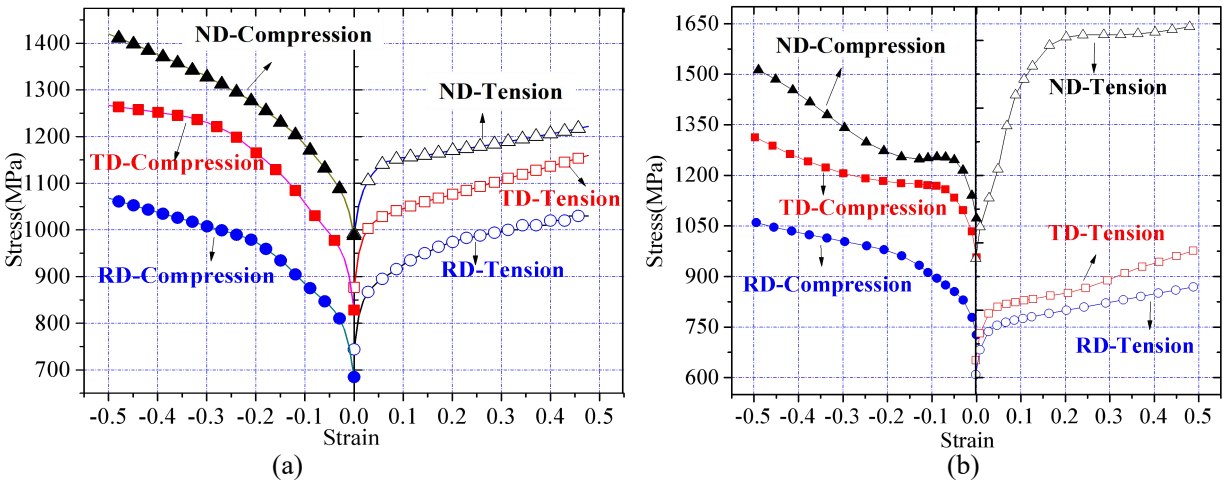

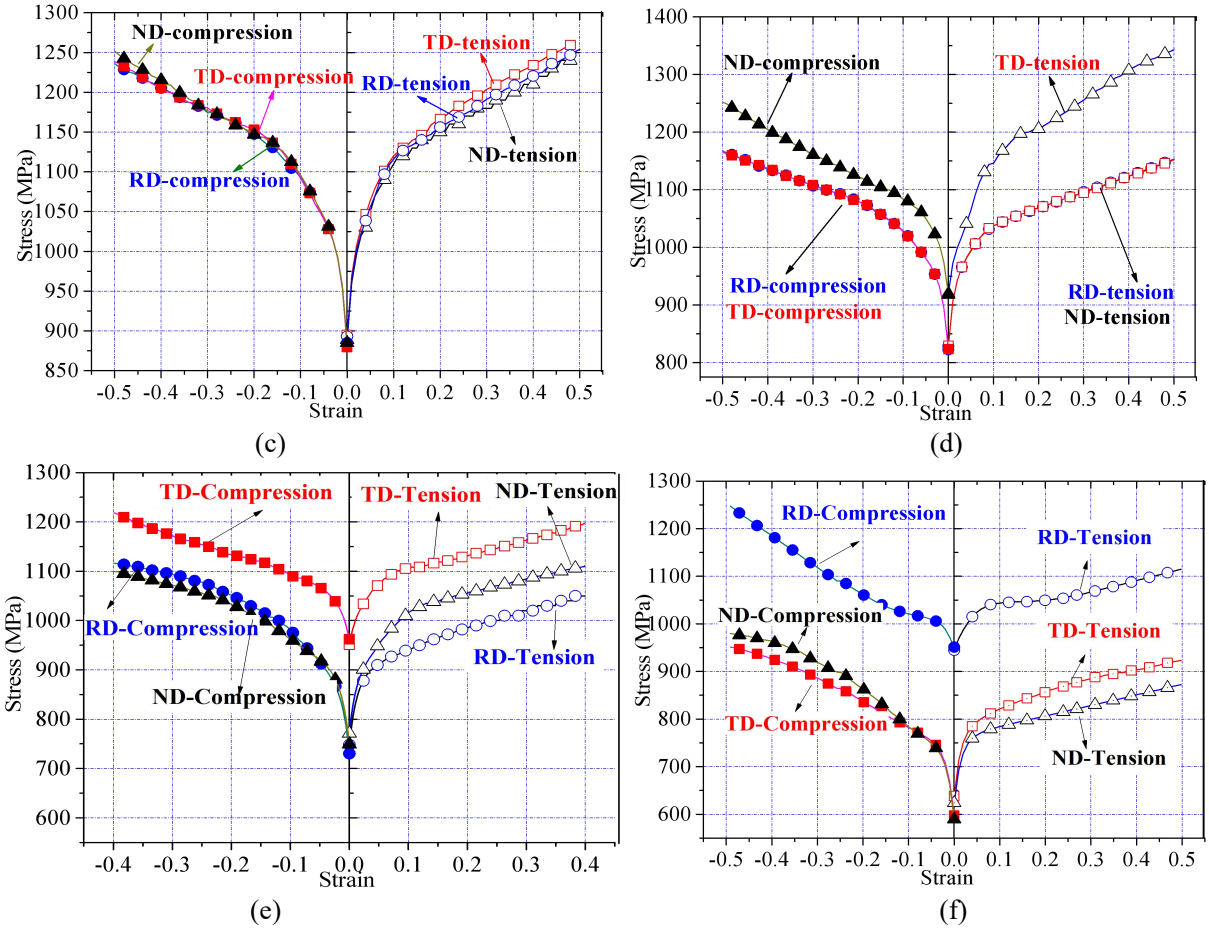


**Fig.15.** True stress-strain curves under different texture conditions: (a) as-received texture; (b) bimodal texture; (c) random texture; (d) radial texture; (e) tangential texture; (f) rolling texture.

### *4.2.2 Anisotropy and asymmetry in plastic strain*

As mentioned in Section 2.2, the CSR is used for characterizing the anisotropy and asymmetry of plastic flow of HSTT. Fig. 16 shows the obvious evolution of CSR-values along RD-tension, TD-tension and RD-compression for different textured samples. Fig. 16(a) reveals that the variation tendency of the calculated CSR-values has a good agreement with the experimental ones presented in Section 2.2. It is confirmed that the CSR is not constant in plastic deformation in most cases. In uniaxial tension, the CSR-value first rapidly decreases then stabilizes with the increase of plastic strain. While, there are totally different or even contrary evolution curves in the uniaxial RD-compression, as shown in Fig. 16(d) and (f). For the rolling texture, the CSR-value in compression increases with strain; However, for the samples with the as-received, bimodal and radial textures, the CSR-values decrease with the increase of plastic deformation; The CSR-values have a little change during deformation for the random textured and tangential textured samples. In addition to the above obvious asymmetry of plastic flow, the pronounced anisotropy of plastic flow is also observed and shown in Fig. 16(a), (b), (e) and (f).

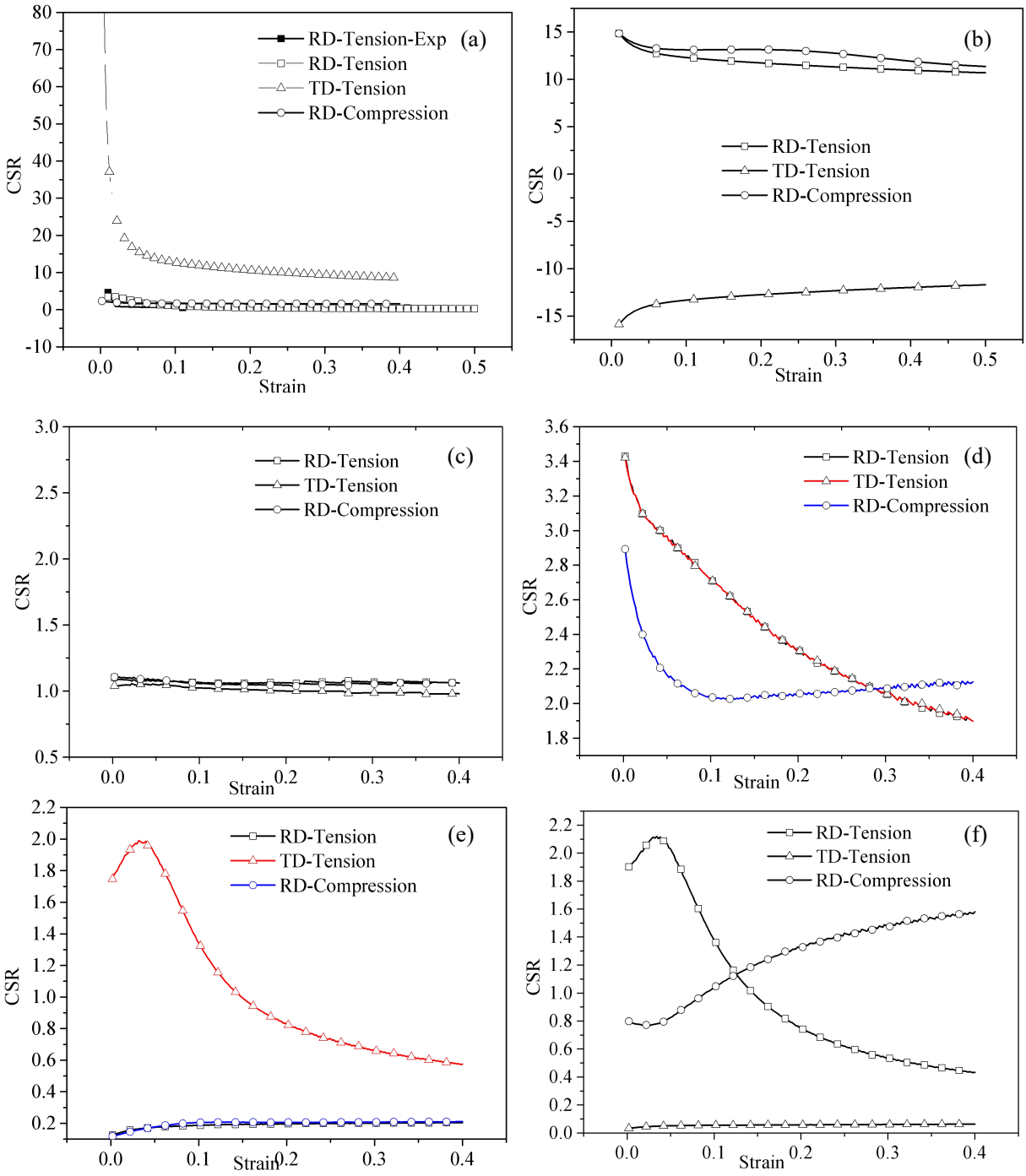


**Fig.16.** Variation of the CSR values under different conditions: (a) as-received texture; (b) bimodal texture; (c) random texture; (d) radial texture; (e) tangential texture; (f) rolling texture.

It is noted that with the RD **deformation**, the CSR-values of the bimodal textured sample are the highest among all the initial textures, and the CSR-values for the tangent texture are the smallest. For the uniaxial tension along RD, the average CSR-values of the as-received texture, bimodal texture, random texture, radial texture, tangential texture and rolling texture are 1.51, 11.70, 1.068, 2.40, 0.51 and 2.5, respectively.

### *4.2.3 Distorted evolution in yield loci*

Using the yield stress data obtained from physical and virtual experiments, the yield loci for the six levels of the accumulated plastic strains are constructed by means of the specific plastic work as shown in Eq. (22).

$$W_P = \int \sigma . d\varepsilon^{pl} \tag{22}$$

The uniaxial tension stress-strain curve in the RD direction is chosen as a reference for plastic work, viz., the yield stresses $\sigma_0$ and the corresponding plastic work $W_p$ are calculated for the particular value of plastic strains $\varepsilon_p^0$. Then at the same plastic work of $W_p$, the yield stress $\sigma_{90}$ for RD compression and TD tension/compression as well as the yield stress components ($\sigma_{45}$, $\sigma_{45}$) for biaxial tension/compression are determined. Following the above procedure, as shown in Fig.17, the yield stress points ($\sigma_0$, 0), (0, $\sigma_{90}$) and ($\sigma_{45}$, $\sigma_{45}$) at different plastic strains of $\varepsilon_p^0$ are thus plotted in the stress space.

The normal anisotropy Hill'48*R* yield function, formulated in Eq.(3), is used to plot the yield loci of the HSTT with different initial textures corresponding to different equivalent plastic strains. Since the response along the hoop direction is difficult to measure for tubular materials, the Hill'48*R* is frequently used for tubular materials in many prior arts (Kuwabara, 2007; Yang et al., 2012). Fig.17 shows that, in addition to the random texture, the distributions of the yield loci are anisotropic and the non-centro-symmetric for most initially textured samples, which indicates the existence of irregular yielding and nonlinear evolution in titanium tubes. It is believed that these distorted plasticity behaviors are explicitly presented by anisotropy and asymmetry in both flow stress and plastic strain in 3D stress state.

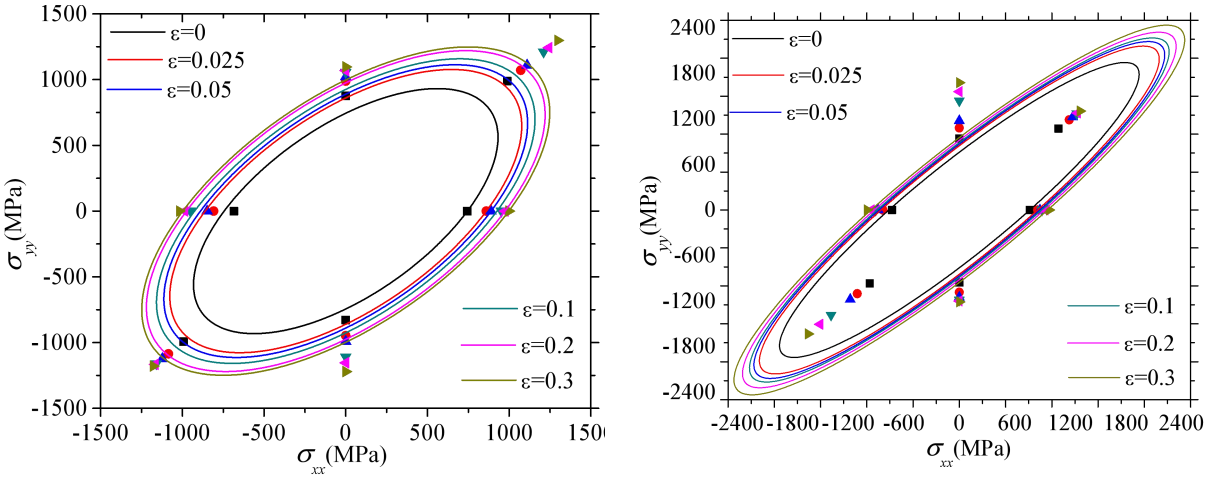

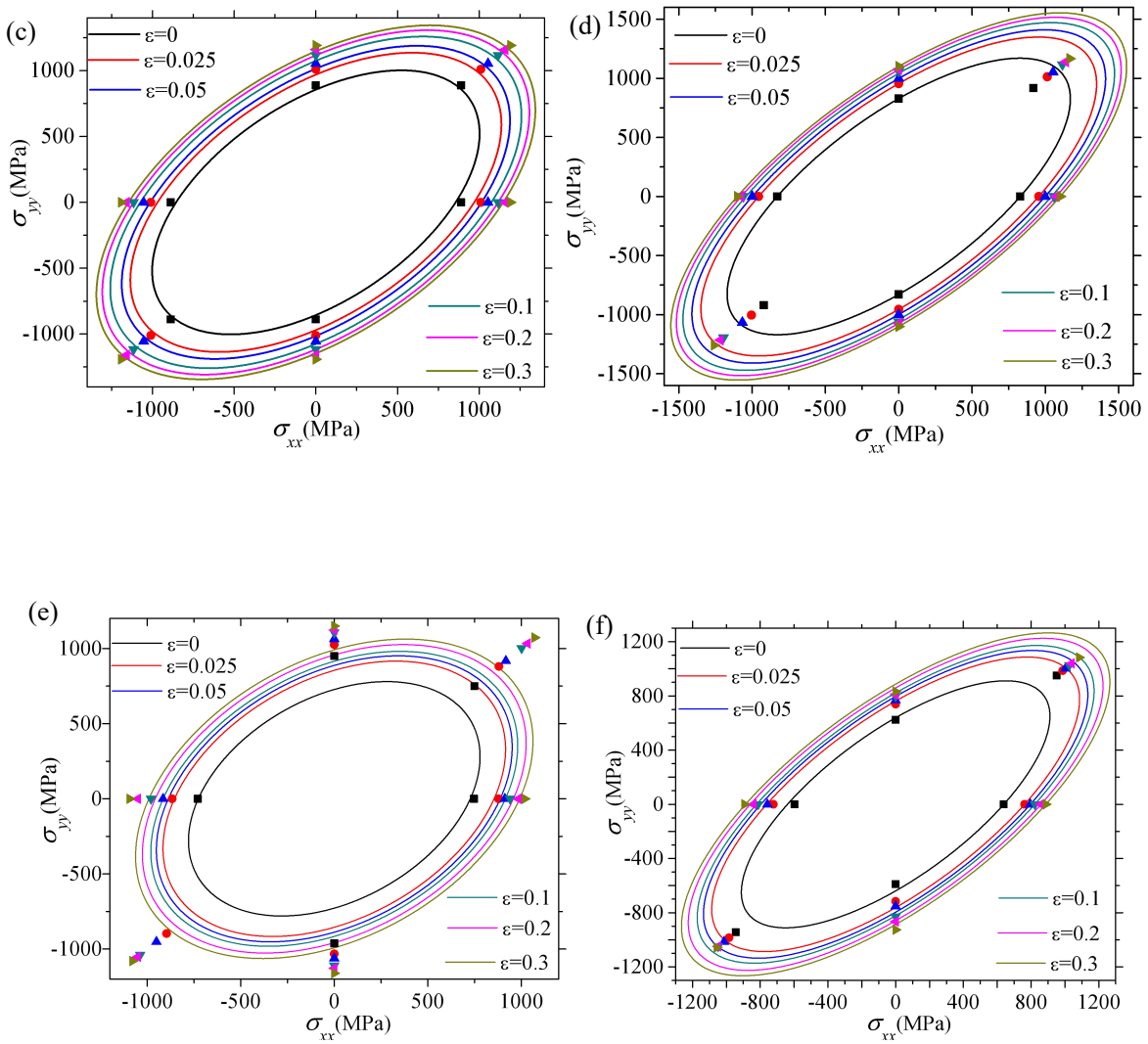


**Fig.17.** Yield loci for HSTT by normal anisotropy Hill'48*R*: (a) as-received texture; (b) bimodal texture; (c) random texture; (d) radial texture; (e) tangential texture; (f) rolling texture (solid lines- predicted yield loci using the Hill'48 orthotropic criterion; symbols- Exp. and VPSC virtual experiments). Same style

There is no figure sub-title of (a) and (b) in Fig.17

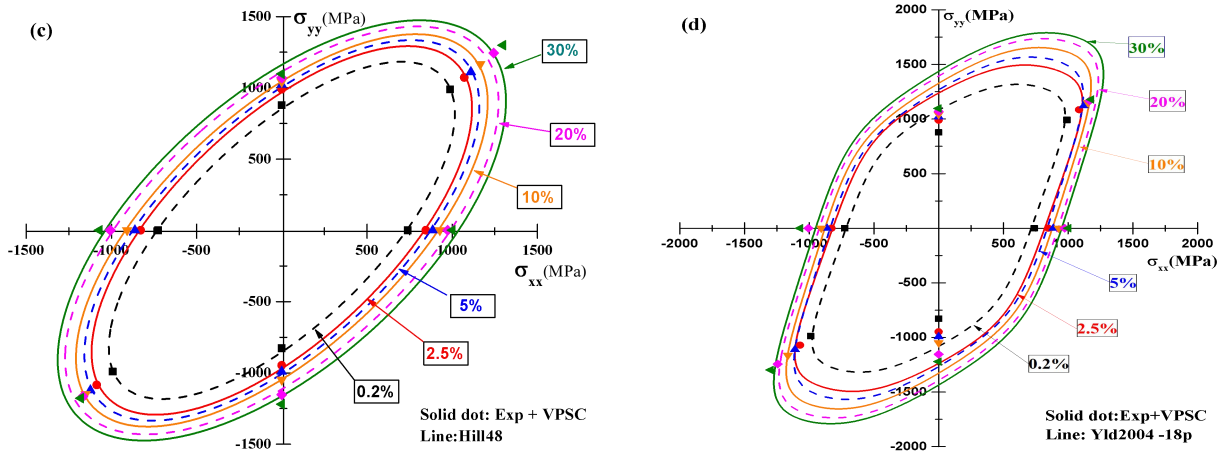

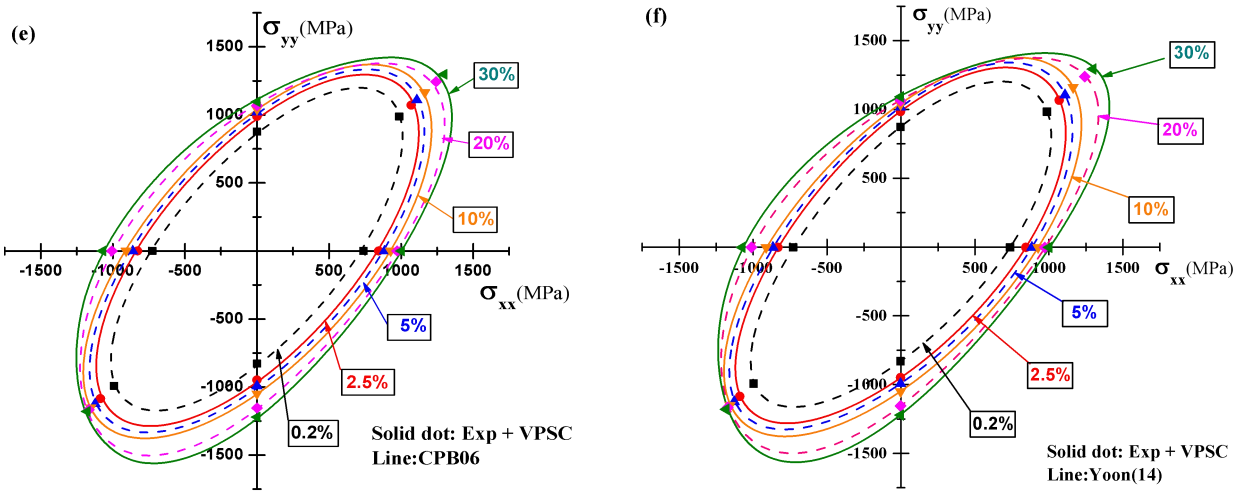


**Fig.18** Yield loci for HSTT with as-received texture using different criterion: (a) Full Hill'48; (b) Yld2004-18p; (c CPB06; (d) Yoon (14)

There is no figure sub-title of (a) and (b) in Fig.18

However, the quadratic feature of Hill'48R yield equation results in incomplete anisotropy and centro-symmetry ellipse, and this most widely used yield criterion cannot capture either the observed anisotropy or the T-C asymmetry of the tubular materials in terms of the yield stress and plastic flow. For comparison, the full Hill'48 criterion and other currently proposed yield criteria, such as Hill'48, Yld2004-18p (Barlat, et al., 2005), CPB06 (Cazacu et al., 2006) and Yoon'14 (Yoon et al., 2014) are considered for describing the anisotropy and asymmetry of the as-received HSTT with the near radial crystallographic reorientation. The detailed calibration procedure by combining the experimental data and the VPSC computation can be referenced in the literature (Li et al., 2016). Fig.18 shows that, compared with the normal anisotropy Hill'48*R* criterion, the full Hill'48 criterion can describe more accurately the distorted plasticity of the HSTT. However, both the full Hill'48 and Yld2004-18p still cannot completely describe the significant evolution of the anisotropy/asymmetry of what??? of the titanium tubes. In general, the yield loci by using the CPB06 and Yoon'14 criteria match well with the experimental and VPSC data.

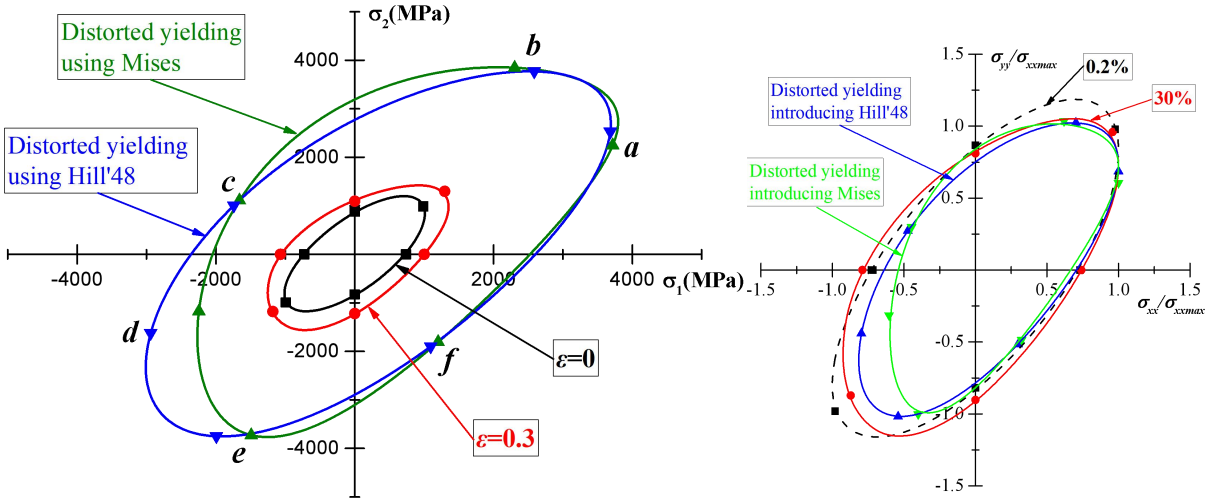


**Fig.19** Comparison of the yield loci a) by Knoop indentation-based method and macro/meso scaled hybrid methodology (Exp.+VPSC); b) the normalized yield loci using different methods.

Furthermore, through comparing, Fig. 19(a) shows that the yield loci calibrated by CPB06 criterion and Knoop indentation-based method can well describe the anisotropy and asymmetry deformation?? behaviors of the as-received tubular materials. The discrepancy between them should be attributed to two reasons: 1) the analytical conversion from the anisotropic hardness information to strength one results in the strength discrepancy; 2) the higher degree of the localized deformation at the surface in the Knoop indentation causes such a strength discrepancy. It is noted that, as shown in Fig.19(b), via comparison of the normalized yield loci, it is found that the shapes of the yield loci generated the Knoop indentation-based characterization method is similar to the shapes of the virtual experimental yield loci, especially in the first quadrant. It is concluded that the revised Knoop hardness test can really provide the qualitative articulation of the nature of yielding of materials.

## *4.3 Mechanisms for coordinating the distorted plasticity*

### *4.3.1 Activities of multiple deformation mechanisms*

By examining the relative activities of individual deformation modes mentioned in Section 2.3, the competitive mechanisms of slipping/slipping, slipping/twinning and twinning/twinning under six typical loading paths are explored for different initially textured HSTT, which provides an insight into the macroscopic behaviors of different textured samples.

For the as-received texture in Fig. 20(a) and (b), both the RD-tension and TD-tension are dominated by prismatic slip (Pr) with a low CRSS over the entire range of plastic strain. Both the tensile twinning (Tt) and the compressive twinning (Ct) remain inactivated throughout the deformation. The deformation along c-axis of the HCP is mainly accommodated by the pyramidal slip (Py<c+a>). Hence, when subjected to tension along RD and TD, the

corresponding flow stress is relatively lower. While, upon the compressive deformation along RD and TD, as shown in Fig.20(c) and (d), although the dominated deformation mechanism still turns to Pr and its activity becomes reduced along the plastic straining, the role of Py<c+a> increases gradually, and contrary to the results of RD-tension and TD-tension, both the tensile twinning (Tt) and the compressive twinning (Ct) activate to accommodate the deformation along the c-axis of the crystal. Relatively, the activity of Ct is far more prominent than that of Tt. It is noted that, the activities of Ct and Tt result in the higher strain hardening rate and flow stress in compression along RD and TD, as shown in Fig. 15(a).

Unlike RD and TD loading, when subjected to deformation along ND, the loading direction is almost parallel to the c-axis of a large fraction of grains. As shown in Fig. 20(e) and (f), the ND-tension and ND-compression are dominated by Py<c+a> with a higher CRSS, and the Pr becomes relatively less activated along the plastic straining. Meanwhile, Ct and Tt are also active similar to those in RD and TD compression deformation. It can be believed that the activities of the Py<c+a>, Ct and Tt result in a higher flow stress along ND deformation, as shown in Fig. 15(a), and enforcing the deformation along the ND of HSTT requires the activation of much harder Ct and Py<c+a> slip to accommodate deformation along the crystal c-axes. As shown in Fig. 15(a), it is noted that the competitive activities between Pr, Py<c+a> and the occurrence of Ct and Tt contribute to the remarkable anisotropy and asymmetry of HSTT, viz., distorted plasticity with strain. For magnesium, it is noted that the Py<c+a> is mostly inactive at room temperature (Mohr et al., 2013), and Basal slip is the dominant mechanism in coordinate the deformation (Jin, et al., 2015).

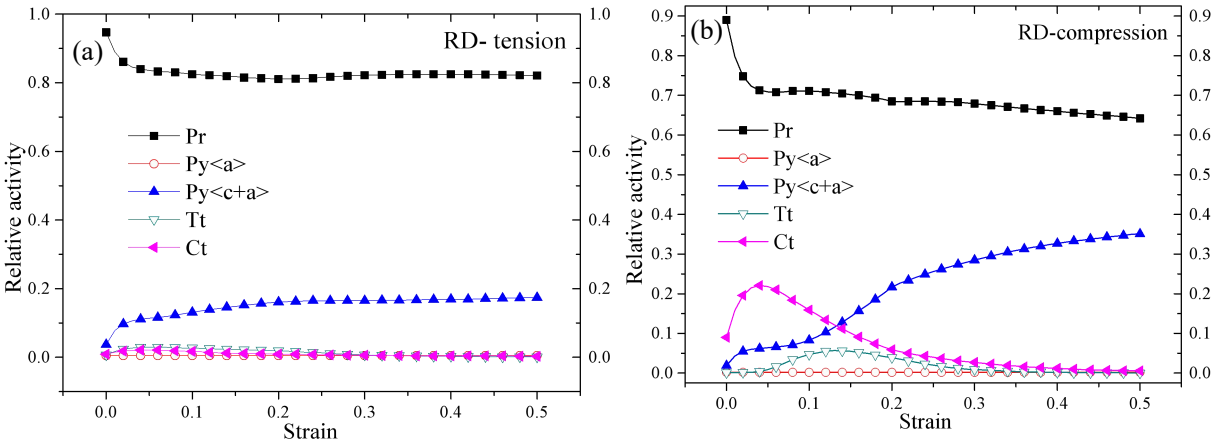

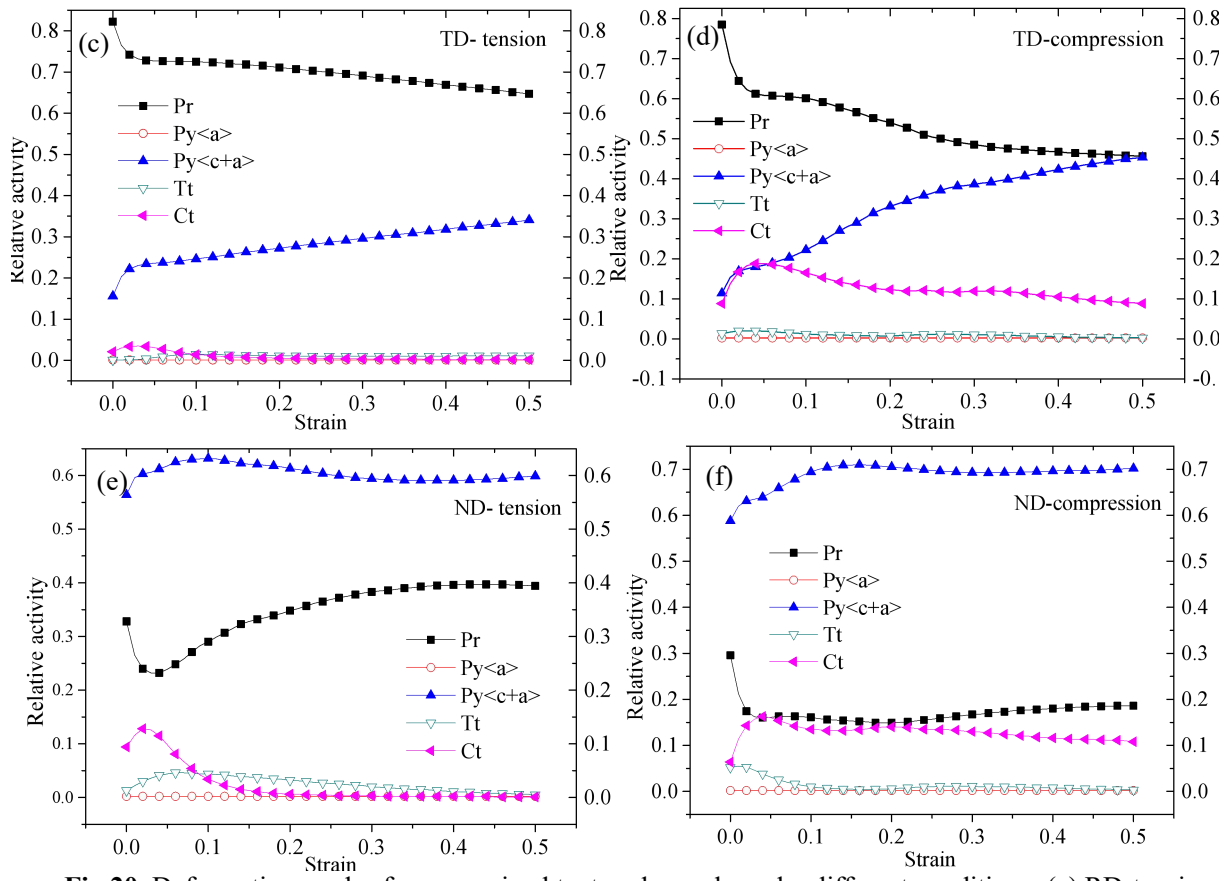


**Fig.20.** Deformation modes for as-received textured sample under different conditions: (a) RD-tension; (b) RD-compression; (c) TC-tension; (d) TC-compression; (e) ND-tension; (f) ND-compression.

The above competitive activities and the coordination of the individual mechanism can be observed for the tubular materials with other initial textures. The distinguished macroscopic responses can be turned to the different relative activities of multiple slipping and twinning modes. For the tube with the initial random texture, the dominant mechanism is Pr and Py<c+a> is a key role to accommodate the c-axis related deformation. Since the relative activities of individual deformation modes for three loading directions are nearly identical, the ideal isotropy and symmetry behaviors are observed and shown in Fig.15 (c), Fig.16 (c) and Fig.17 (c). It is worth noting that, as shown in Fig.21, when the loading direction is parallel to the c-axis of the low symmetry HCP crystal, the role of the Py<c+a> becomes overwhelming. In addition to the compressive twins Ct, the tensile twin Tt becomes extraordinary abundant to accommodate the c-axis deformation at the early deformation stage. The roles of both the Ct and Tt weaken gradually to induce more Pr and Py<c+a> slipping activities at the later deformation stage. As shown in Fig.15, the observed concaved hardening response frequently occurs when the loading direction is parallel to the c-axis of the HCP crystal. The root cause can be traced by the above unique physical mechanisms, viz., a greater fraction of tensile twinning Tt at lower plastic strain followed by slip and strain hardening at the higher level of deformation.

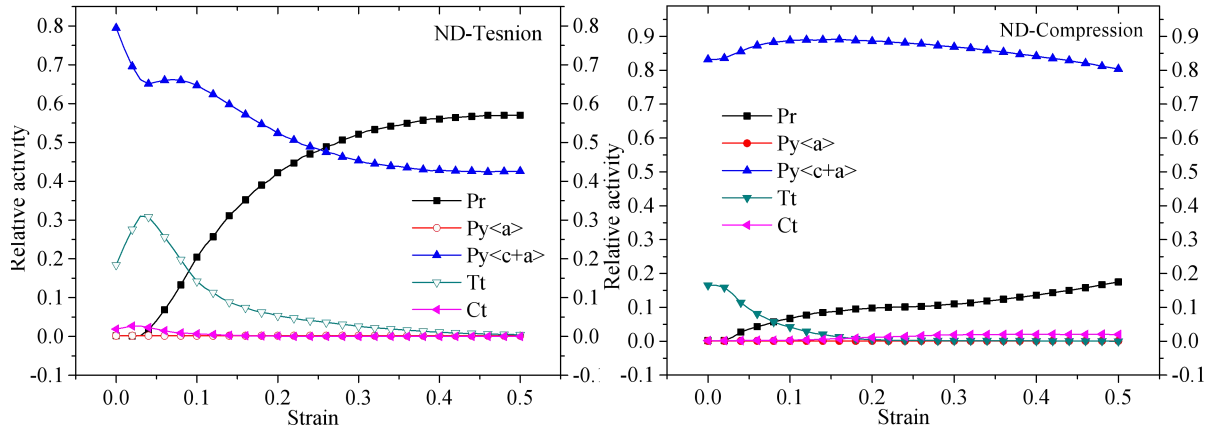


(a) ND-Tension for bimodal texture




(b) ND-Compression for bimodal texture

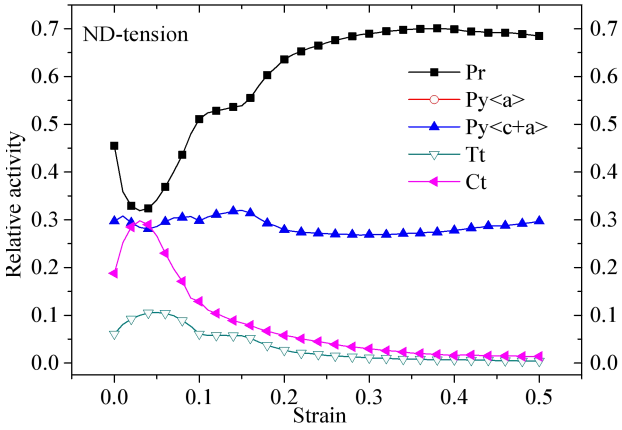


(c) ND-Tension for radial texture

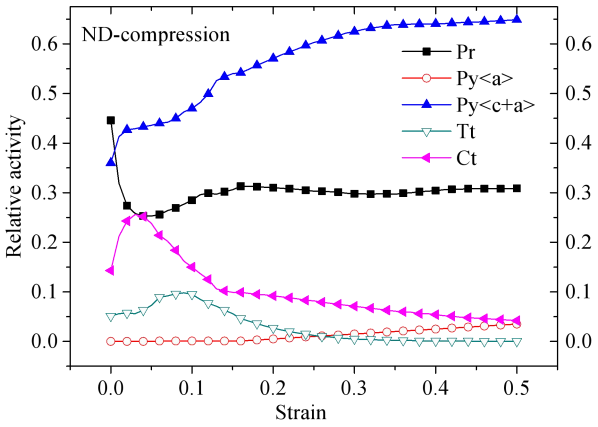


(d) ND-Compression for radial texture

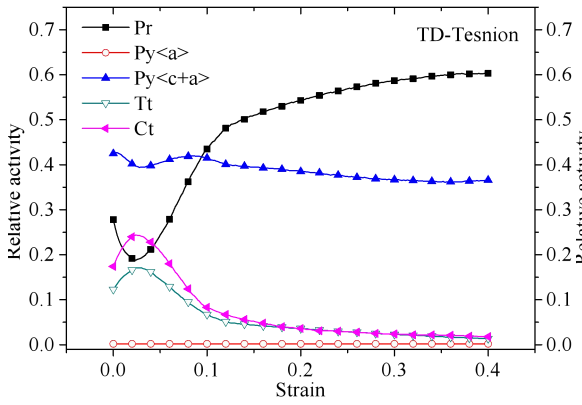


(e) TD-Tension for tangent texture

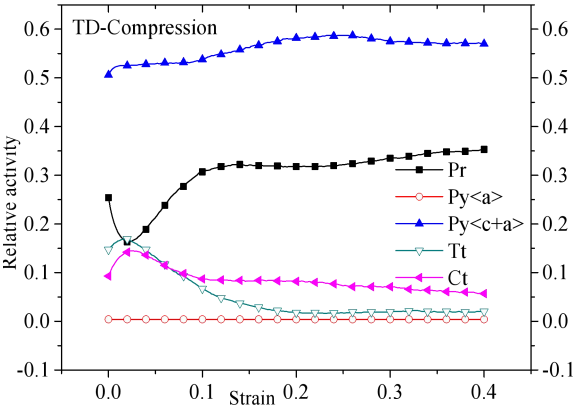


(f) TD-Compression for tangent texture

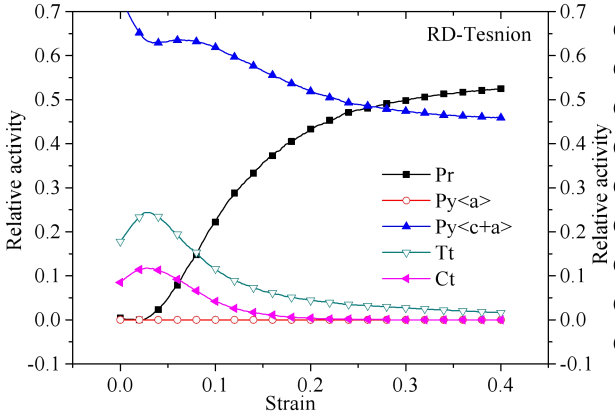


(g) RD-Tension for rolling texture

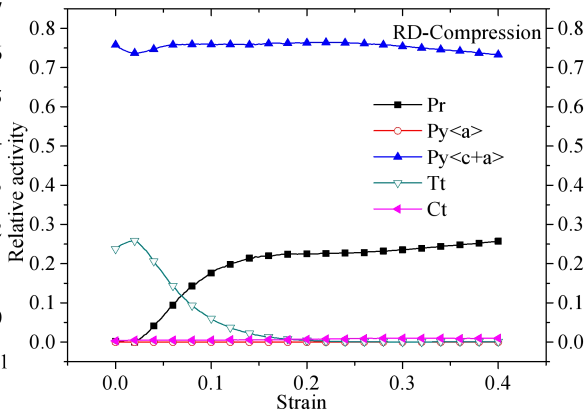


(h) RD-Compression for rolling texture

**Fig.21.** Deformation mechanism for other textured samples under different conditions.

### *4.3.2 Texture evolution*

The above slipping/slipping, slipping/twinning and twinning/twinning coordination surely induce diverse texture evolution along plastic strain for each textured tube, which is the root cause of the distorted evolution of the plasticity mentioned in Section 4.2. Table 5 shows the different texture evolution of the tubes with six different initial textures under six typical loading conditions. By comparing basal pole figures, the interaction between deformation mechanisms and grain reorientation can be explained. The discussion is focused on the as-received one.

**Table 5.** Predicted Basal pole distributions after 40% tension/compression along six directions for six initial textured tubes.

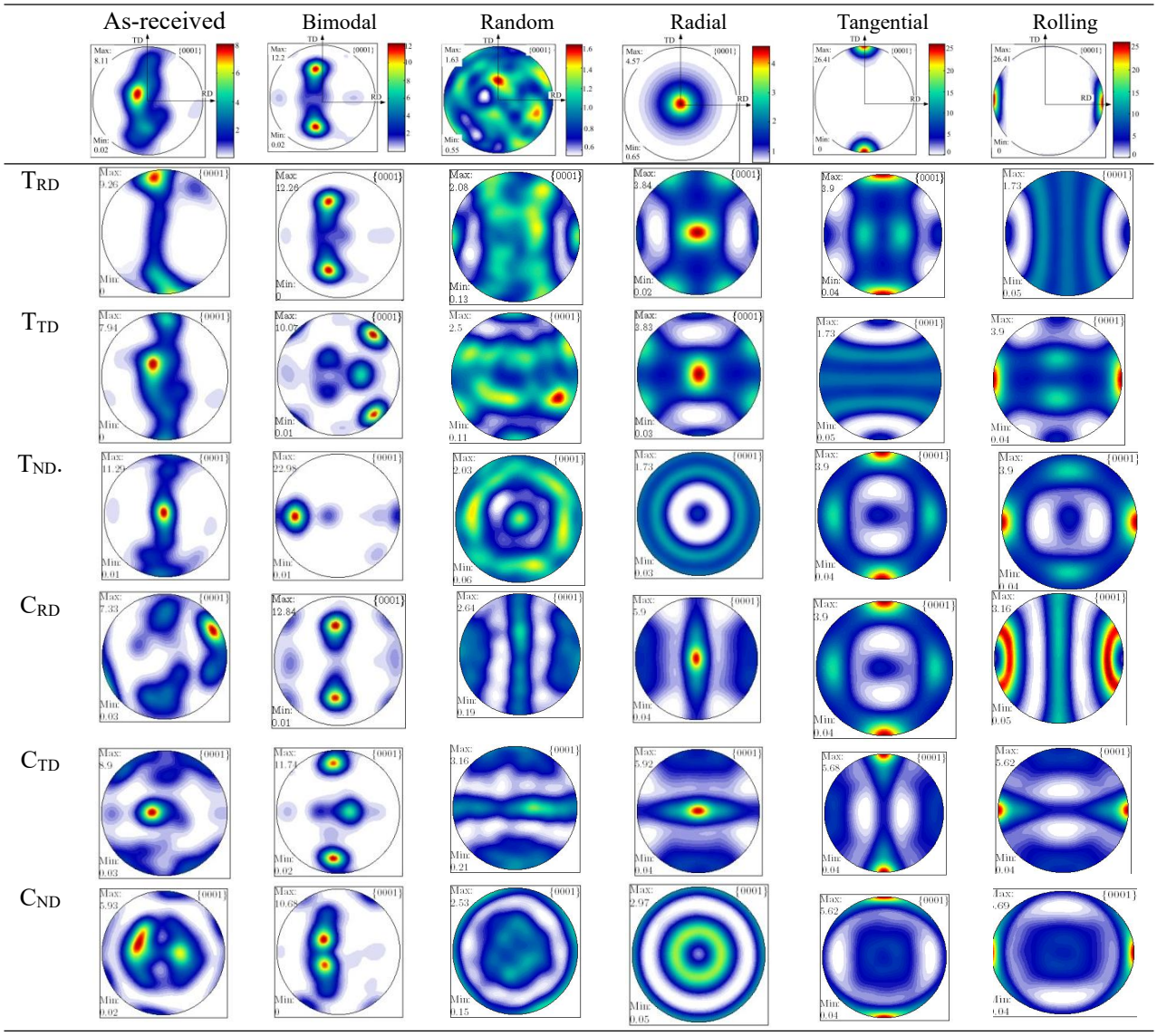


As for the as-received samples, the pole figures reveal a dramatic texture variation when subjected to the compression along RD, TD and ND. In addition, Ct and Tt play a dominant role in allocating the texture evolution of the RD, TD and ND compressed samples in Fig.20 (b), (d)

and (f). While, for the tension along RD, TD and ND, a relatively less variation of the crystal reorientation is observed except for the tendency of the tangent texture to some extent. As shown in Fig.21, there is negligible twinning occurrence through the entire deformation stage for the tensile deformation along three directions. Thus, the role of the twinning in reorienting the crystallographic texture and coordinating the deformation modes for benefiting the dominant slipping systems such as Py<c+a> is further confirmed though their fraction is smaller compared with those of the slipping systems.

Regarding the compression along ND, as shown in Fig.20, the dominant pyramidal<c+a> slip occurs to accommodate the c-axis related deformation coordinated by Ct and Tt. The pyramidal<c+a> reorientation creates a fiber perpendicular to the tensile direction and this joint mechanism rotates the c-axes away from the tensile direction, viz., basal poles have a tendency to align themselves parallel to the direction of the maximum compressive strain. The maximum compressive strain direction is ND. However, the Ct {11-22}<11-2-3 rotates the basal pole away from the center of the pole figure. By means of this rotation in the twinned structure, an orientation tilted 50°-90° away from ND direction is usually achieved (Tenckhoff, 2005). The coupling effects of the Py<c+a> and Ct for accommodating the c-axis related deformation cause the tangent texture to tend to disappear and gradually form the radial texture with the highest pole density tilting away 30° from the ND. As for the compression along TD, since the Py<c+a> is not the dominant mechanism to accommodate the c-axis deformation, the initial tangent texture has not been eliminated thoroughly. Furthermore, as for the compression along RD, the fraction of the Py<c+a> activity is small, and the activation of tensile twins causes a nearly 90° rotation of crystal structure about the <1-120> directions on the {10-12} planes toward the center of pole figure. The coupling effects of Py<c+a>, Ct and Tt thus result in the combination of the tangent texture and rolling texture.

### *4.4 Tube texture tailoring by positively control of full plastic flow*

The above discussions prove that the distorted plasticity of HSTT depends on the loading conditions and the initial/evolution of texture, and the loading conditions result in abrupt texture variation and distorted behaviors for the given initial textures. To obtain high performance titanium tubular parts beyond the shaping, for the tubes with certain initial texture, by positively allocating the plastic flow in 3D spatial space, the finished product with preferred formability/performance can be tailored with desired textures. Taking the tube with the initial random texture as a case, the relationship between full plastic flow and texture evolution is explicitly established, and then the multi-pass cold rolling process is designed to allocate the

spatial flow of the plastic strain to induce the desired texture.

### *4.4.1 Relationship between plastic flow and texture evolution*

Due to the arbitrary change in both the diameter and wall thickness, the plastic flow of tubular materials is more complicated to be characterized than that of the rolled sheet. Instead of *Rd* and *Q* as shown in Eqs.(23) and (24) (Lebensohn et. al.,1996), a more general index is used to represent the spatial plastic flow and the deformation degree of tubular materials.

$$Rd = \frac{A-a}{A} \times 100\% = \left\{ 1 - \left( \frac{t}{T} \right) \left( \frac{d}{D} \right) \right\} \times 100\% \tag{23}$$

$$Q = \frac{\ln\left( t/T \right)}{\ln\left( d/D \right)} = \frac{\varepsilon_r}{\varepsilon_\theta} \tag{24}$$

where *a* and *A* are the cross-section areas of the reduced tube and tube billet, *t* and *T* are the wall thicknesses of the reduced tube and tube billet, respectively; *d* and *D* are the mean diameters of reduced tube and the tube billet, respectively.

As shown in Fig.22 and according to the law of volume constancy and the principal strain of tube, the principal strains for the rolling, tangential, and radial directions denoted as $\varepsilon_z$, $\varepsilon_\theta$, and $\varepsilon_r$, respectively, can be drawn on a plane triaxial strain diagram. Any change in the tube dimensions can be represented by a strain vector in the above plane triaxial strain diagram. The size and angle of the strain vector correspond directly to the deformation degree and the plastic flow mode As expressed by Eqs.(25) and (26), the size and angle of the strain vector are defined by effective strain $\varepsilon_e$ and strain ratio $\alpha$. The strain ratio refers to an angle clockwise from the positive $\varepsilon_z$ axis to the direction of the strain vector shown in Fig.22.

$$\varepsilon_e = \sqrt{\frac{2}{3}\left( \varepsilon_r^{\,2} + \varepsilon_\theta^{\,2} + \varepsilon_l^{\,2} \right)} \tag{25}$$

$$\alpha = \arctan[(\varepsilon_\theta - \varepsilon_r)/\sqrt{3}\varepsilon_l] \tag{26}$$

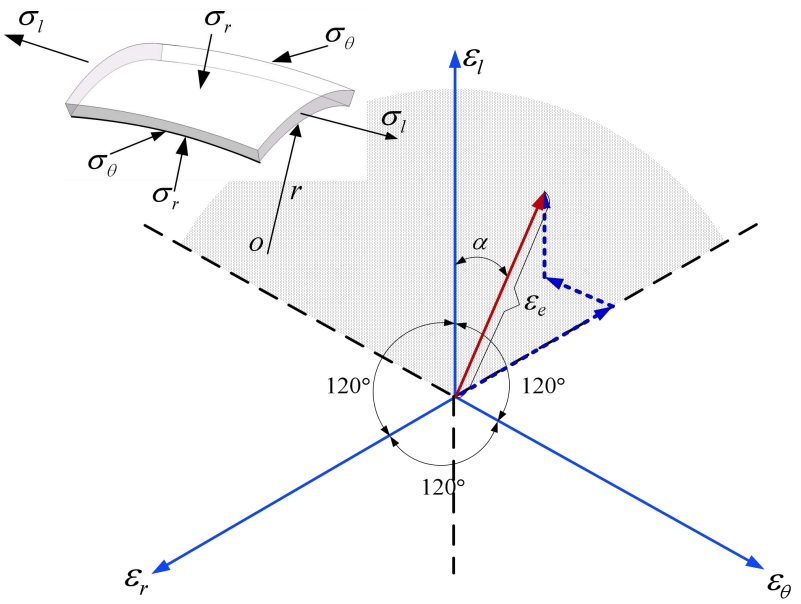


**Fig.22.** Plane triaxial strain diagram with strain vector.

To investigate the relationship between plastic flow and texture evolution, the strain vectors for the initial random textured tube under six fundamental loading conditions are calculated using Eqs. (23) and (24). Table 6 shows the texture evolution with different strain vectors. When the strain ratio is about $60°$, the wall thickness reduction is the dominant deformation mode, and the radial texture is gradually formed along the plastic straining; When the strain ratio is about $120°$, the diameter expansion is the dominant deformation mode, and the rolling texture is formed; When the strain ratio is about $-60°$, the diameter reduction is the dominant one, and the tangent texture is formed. Based on Table 5, by plotting the texture evolutions with different strain vectors ($\varepsilon_e$, $\alpha$), an equilateral triangle can be constructed and presented in Fig. 23. For symmetry, the triangle is completed with another three moderate textures and they fall on the vertical line through the centre of the triangle. The centre is marked with a pole figure indicating random texture. It is clear that the radial texture can be obtained with the stain ratio ranging from $0°$ and $60°$, and the tangent texture can be tailored with the strain ratio ranging from $0°$ and $-60°$. The density of the above texture increases gradually with the plastic strain.

**Table 6.** Strain vector and texture evolution of tube under different loading conditions.

| Deformation path | Range of strain ratio $\alpha$ | Deformation mode of tube | Texture of tube when $\varepsilon_e$=0.2 | Texture of tube when $\varepsilon_e$=0.4 |
|---|---|---|---|---|
| RD-tension Q=1 | -1.62° ~ -0.91° | Length elongation with equal wall thinning and diameter contraction | 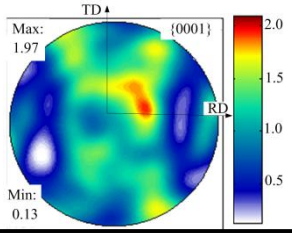 | 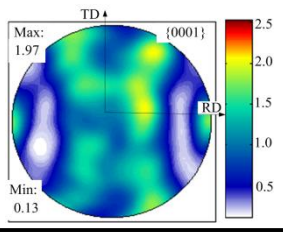 |

| | | | | |
|---|---|---|---|---|
| TD- tension<br>-1<Q<0 | 119.7° ～<br>120.6° | Diameter expansion with equal length shortening and wall thinning | 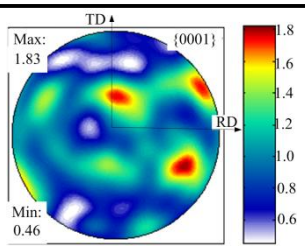 | 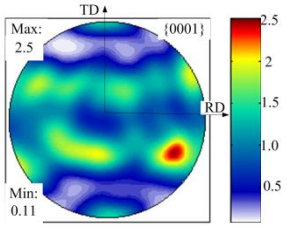 |
| ND- tension<br>Q<-1 | -118.1° ～<br>-119.2° | Wall thickening with equal diameter contraction and length shortening | 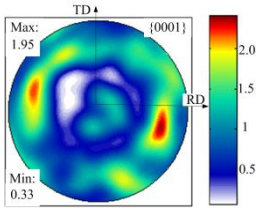 | 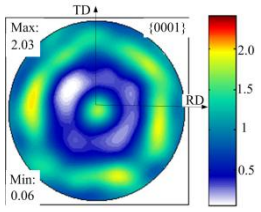 |
| RD- compression<br>Q=1 | 178.32° ～<br>179.09° | Length shortening with equal wall thickening and diameter expansion | 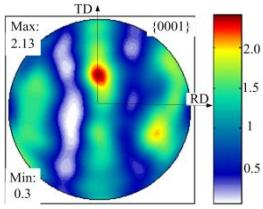 | 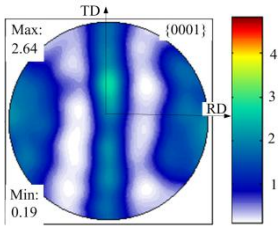 |
| TD- compression<br>-1<Q<0 | -60.9° ～<br>-60.1° | Diameter contraction with equal length elongation and wall thickening | 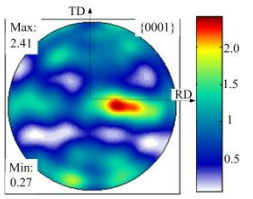 | 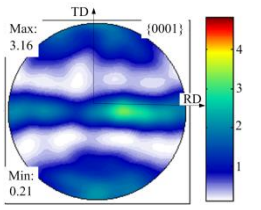 |
| ND- compression<br>Q<-1 | 60.0° ～<br>61.4° | Wall thinning with equal diameter expansion and length elongation | 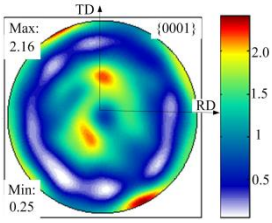 | 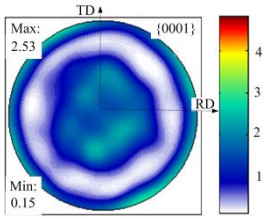 |

Note: The deformation mode of tube is defined by changes in wall thickness, diameter and length.

### *4.4.2 Texture tailoring in cold rolling of HSTT*

As shown in Fig.24, the multi-pass cold pilgering is one of the most widely used fabricating processes for seamless tube with both inner radius and wall thickness progressively reduced between a fixed asymmetric mandrel and forward-and-backward rolling grooved die. The process consists of several tens of "stokes" between which the tube is turned (by 50-60°) and moved forward by a small distance. As mentioned in Introduction, the transient inhomogeneous deformation in cold pilgering results in a great variation in crystallographic orientation, which may induce distinguishable mechanical properties such as elongation, yield strength and ductility (Abe and Furugen, 2012). By taking the process of $\phi 32\times 3mm \rightarrow \phi 17.48\times 1.07mm$ ($\varepsilon_e = 1.6$) with the initial random texture as an objective and according to the above relationship

between strain vector and texture evolution, the process of the multi-pass cold pilgering is designed to tailor the desired texture. The radial texture is regarded as the preferable one for avoiding cross-section flattening because of high resistance along ND direction. Thus, the near radial texture is the target texture for texture tailoring.

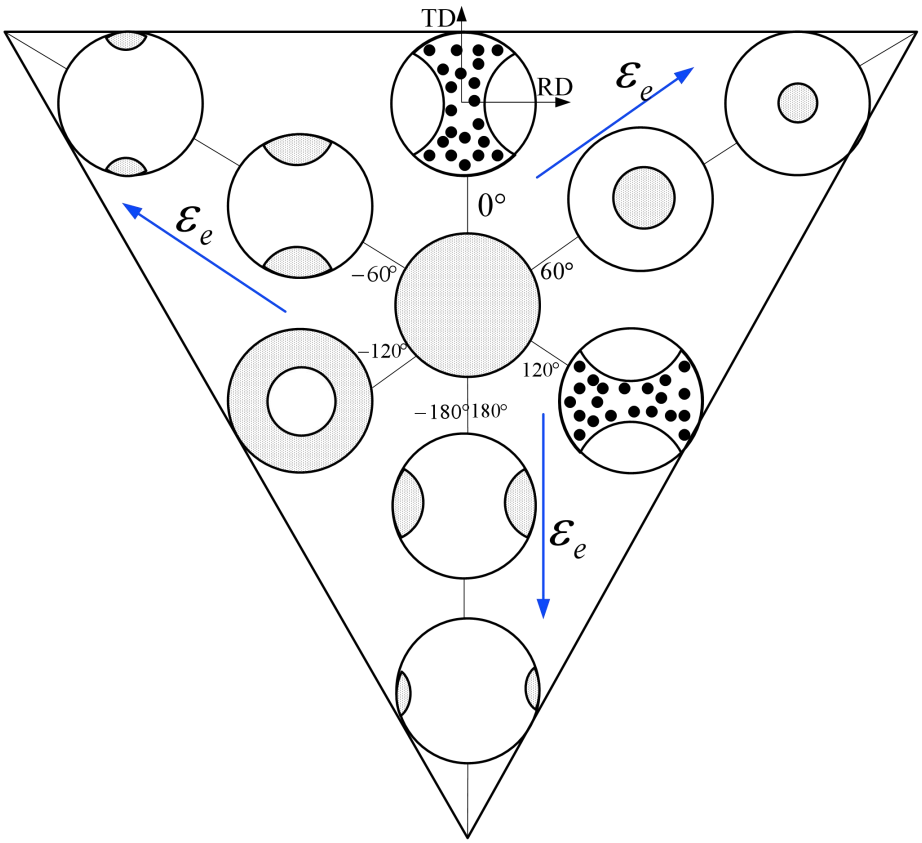


**Fig.23.** Position of texture in relation to the equilateral triangle.

The calibrated VPSC model combined with 3D explicit FE simulation is utilized to predict the texture evolution during cold rolling. Due to the non-proportional and non-steady incremental deformation alternatively in tension and compression during cold pilgering, the boundary condition of tube cold pilgering cannot be accurately described by a monotonic velocity. As mentioned in Section 3.2, the explicit 3D-FE simulation combined with Abaqus/Vumat subroutine is used to obtain the deformation gradients, and then the fully variable velocity gradients of the whole pilgering can be calculated for VPSC input by using Eq. (17). The details on the multi-pass cold pilgering modeling can be found in the report (Li et al., 2013).

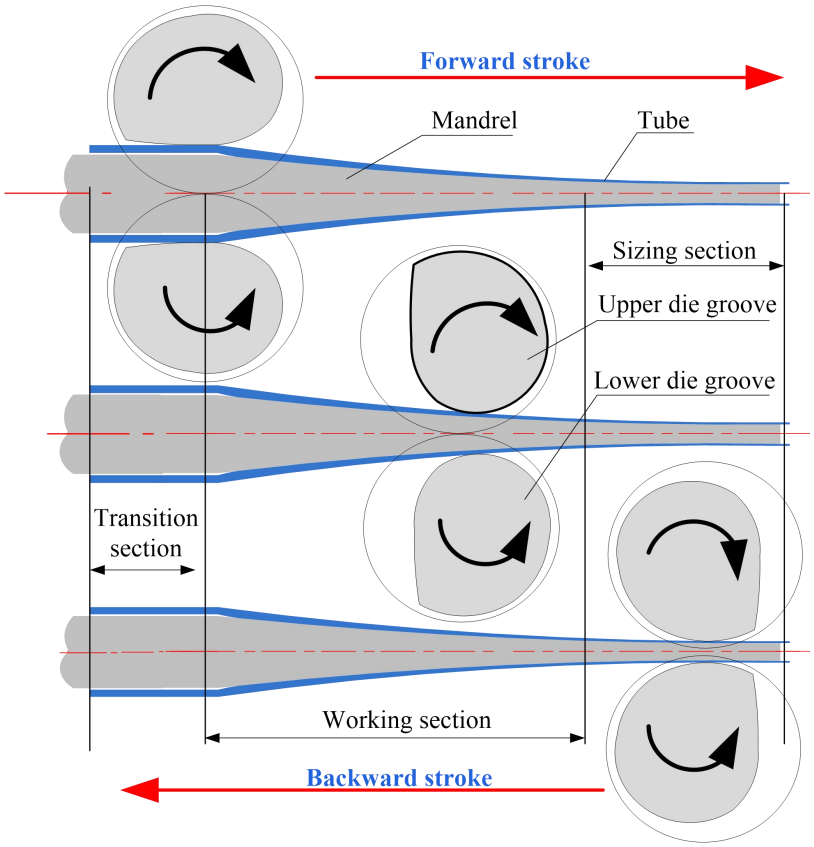


**Fig.24.** Multi-pass cold pilgering of HSTT.

The relationship between strain vector and texture evolution, as presented in Section 4.3.2, shows that the compressive forces of radial direction result in the preferential orientation of the basal poles in radial direction (ND). According to Fig.23, the strain ratio should be within $0° - 60°$ with an enough larger effective strain for the radial texture. Thus, both the pilgering tooling and reduction parameters are designed to obtain the dominant compression deformation along wall thickness compared with the deformation along the tangent direction of the tube. Fig.25 shows the evolution of both the texture and the strain ratio during one-stroke cold pilgering. The A-F represents the different locations on the rolled tube billet along the axial direction, viz., 50, 125, 300, 350, 500 and 600 mm.

It is found that, in the diameter reduction zone (axial location 0-100mm), the tube billet is pressed by the groove and the contraction along the tangent direction, resulting in an obvious hoop reduction strain along with increase of wall thickness, which further causes the strain ratio of about $-60°$ and thus tangent texture ( c-axis of the HCP // tangent direction of tube). In the first stage of wall thickness-diameter reduction (axial location 100-250 mm), the tube billet gradually contacts with the mandrel and the a remarkable wall thickness reduction occurs under the coupling constraints of the grooves and the mandrel, and then the strain ratio quickly increases to about $60°$ with the obvious radial texture (c-axis of the HCP // radial direction of

tube). In the later stage of wall thickness-diameter reduction (axial location 250-600mm), the diameter reduction increases a little and the strain ratio decreases and then stabilizes within the range of 10° - 20° , which causes the tilting of c-axis towards radial direction and tangent direction and finally strong radial texture can be formed with the dominant thickness reduction.

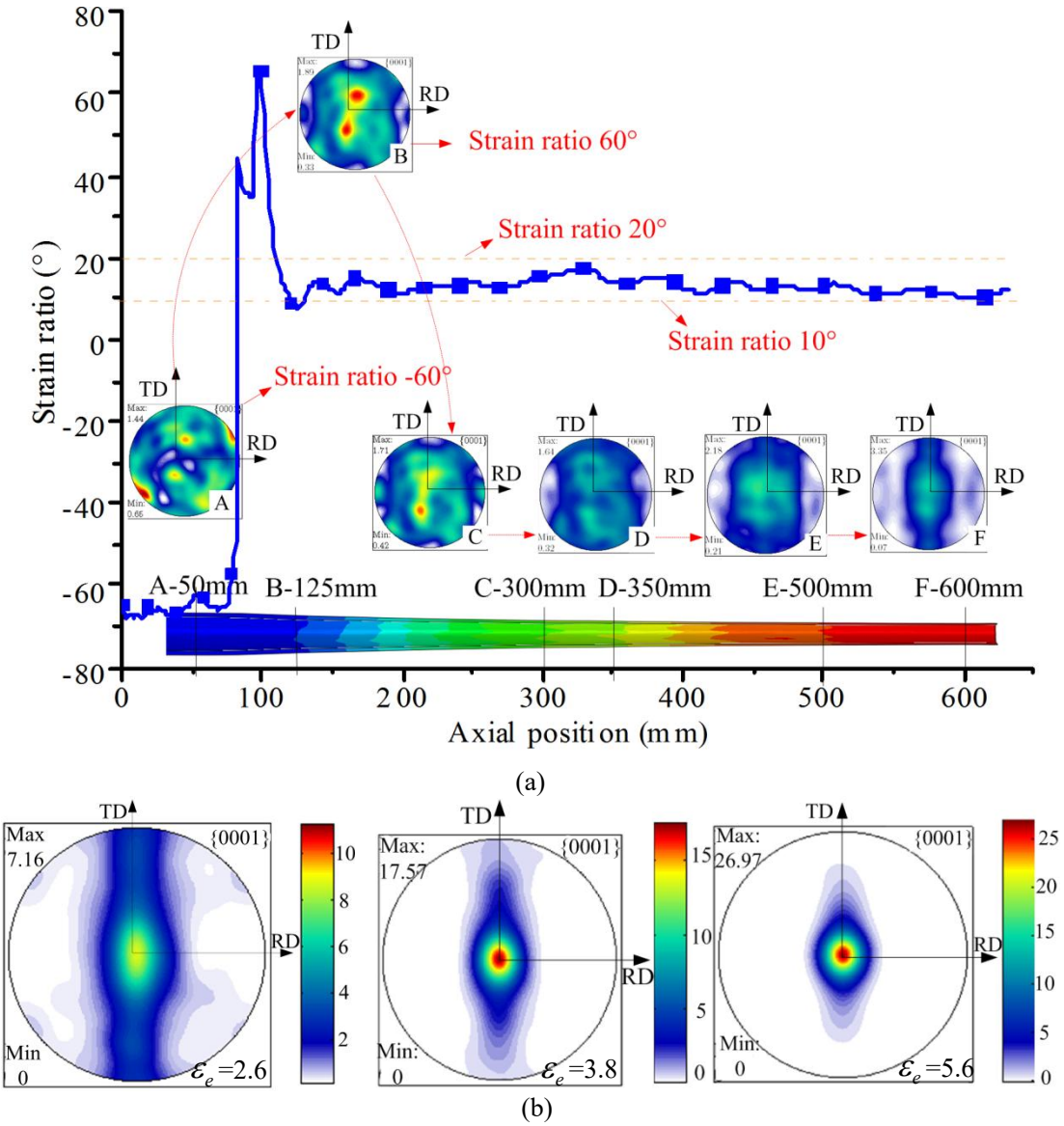


**Fig.25.** Texture evolution of the random texture tube during cold pilgering: (a) with different strain ratios; (b) with different effective strains.

As for the above one-stroke rolling process, the effective plastic strain equals 1.6. However, in practical process, multi-pass design is needed for the finished tube fabrication since enough deformation degree should be satisfied for tailoring the final texture as shown in Fig. 25(a). Hence, the texture evolution with different effective plastic strains including 2.6, 3.8 and 5.6 is quantitatively presented as shown in Fig.25 (b). It can be confirmed that the density of the radial texture for the finished tube increases greatly. Thus, to obtain the dominant radial texture for the

tubes with the initial random texture, the accumulated effective plastic strain should reach up to 3.8 by multi-pass cold pilgering rolling.

In addition to the random texture, the evolutions of two typical initial textures of HSTT, viz., radial texture and extrusion texture, during cold pilgering with different effective strains, are presented as shown in Table 7. To obtain the ideal bimodal texture for the tubes with the initial radial texture, the accumulated effective plastic strain should reach up to 5.6 by multi-pass cold pilgering rolling. For the initial extrusion texture, to obtain the dominant radial texture, the accumulated effective plastic strain should reach up to 3.8. And to obtain the bimodal texture, the accumulated effective plastic strain should reach more than 5.6.

**Table 7.** Texture evolution with different effective strains during cold pilgering: (a) initial radial texture; (b) initial extrusion texture.

| *Routine* | $\varepsilon_e = 0$ | $\varepsilon_e = 2.6$ | $\varepsilon_e = 3.8$ | $\varepsilon_e = 5.6$ |
|---|---|---|---|---|
| *a* | 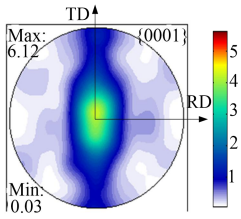 | 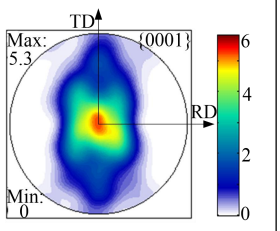 | 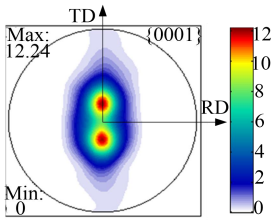 | 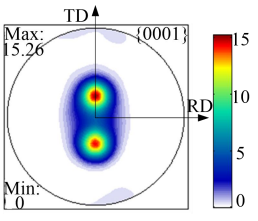 |
| *b* | 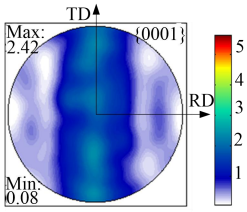 | 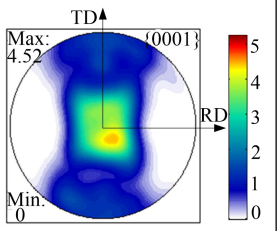 | 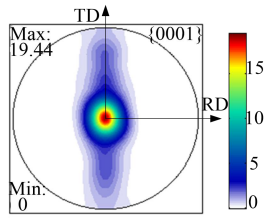 | 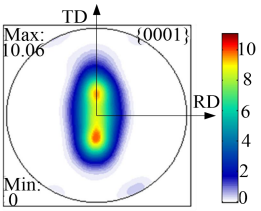 |

## 5. Conclusions

Taking a high strength cold rolled titanium tube as a case, the coupling contribution of anisotropy and asymmetry to the distorted plasticity of titanium tube as well as the underlying mechanisms are quantitatively explored and articulated experimentally and numerically. A quantitative correlation between initial texture, loading condition, distorted plasticity and texture evolution is established to achieve the integrated design of fabricating and forming of titanium tubular products with high dimensional accuracy and satisfied properties. The main contents and results are summarized as follows: Hill? Evolution

1) A hybrid methodology is used to quantitatively investigate the anisotropic and asymmetrical plasticity behaviors and physical mechanisms of tubular materials. By using elaborately designed uniaxial tension/compression experiments of tubular specimens and EBSD analysis, the slip/twinning dominated multiple mechanisms to accommodate the inhomogeneous plastic

deformation are identified; A compression-based orthogonal inverse method is used to calibrate the parameters involved with VPSC theory and the VPSC-based computation with static and variable velocity gradients is conducted under different loading scenarios for predicting the deformation behaviors and texture evolution during various loading conditions including complex forming processes such as multi-constrained tube bending and cold pilgering.

2) The coexistence and competition of the multiple mechanisms such as slip/slip and slip/twinning as well as twinning/twinning result in the remarkable and varied anisotropy and asymmetry characteristics in hardening, strain flow and yield loci for alpha titanium tube in plastic deformation, viz., three slips including prismatic slip Pr<a>, pyramidal slip Py<a> and pyramidal slip Py<c+a>, and two twinning modes including tensile twinning Tt {10-12}<10-1-1> and compressive twinning Ct {11-22}<11-2-3>; The superposition of both anisotropy and asymmetry further results in severe distorted yielding and plastic flow as well as strong irregular evolution of yield loci in 3D spatial stress space, which cannot be described by general yield functions such as Hill'48R criterion.

3)The history of slip/twinning activity determines the texture evolution in the deformed samples, viz., when the loading direction is parallel to the c-axis of alpha titanium, the dominated slip mechanism is Py<c+a>, the second one is Pr<a>, and the relative contribution of twinning to plastic strain is more smaller than that by slip, while it coordinates the texture evolution more greatly; By using more general index strain vector in full spatial space, the relationship between final texture evolution and plastic flow modes is recognized for tailoring the texture evolution, viz., the radial texture can be obtained with a large effective plastic strain and the stain ratio ranging from $0°$ and $60°$; By using this relationship, the finished high strength titanium tubes with the desired textures can be tailored by allocating the plastic flow in 3D spatial space during multi-pass cold pilgering. However, although the radial texture is assumed to be target one, which texture is the preferred one for better formability and higher performance needs further investigation and confirmation.

## Acknowledgements

The authors appreciate the reviewers for their constructive suggestions, Dr. R. Lebensohn of Los Alamos National Laboratory for the access of VPSC code and Miss R. Han and Mr. S. Wang in Northwestern Polytechnical University for Knoop indentation tests. The authors thank the National Science Fund for Excellent Young Scholars (51522509), the National Natural Science Foundation of China (51275415), the EU Marie Curie Actions - MatProFuture Project

(FP7-PEOPLE-2012- IRSES-318968) and the 111 Project (B08040) for the support.

## References

Abe, H., Furugen, M., 2012. Method of evaluating workability in cold pilgering. J. Mater. Process. Technol. 212(8), 1687-1693.
Abdolvand, H., Daymond, M. R., 2012. Internal strain and texture development during twining: comparing Neutron Diffraction Measurements with Crystal Plasticity Finite-element approaches. Acta Mater. 60, 2240-2248
Agnew, S. R., Duygulu, Ö., 2005. Plastic anisotropy and the role of non-basal slip in magnesium alloy AZ31B. Int. J. Plasticity 21**,** 1161-1193.
Amateau M F, Hanna W D., 1975. Comparison of first quadrant yield loci for Ti-6Al-4V with those predicted by Knoop hardness measurements. Metal. Mater. Transac. A 6(2),417-419.
Balasubramanian, S., Anand, L., 2002. Plasticity of initially textured hexagonal polycrystals at high homologous temperatures: application to titanium. Acta Mater. 50: 133-148.
Banerjee, D., Williams, J.C., 2013. Perspectives on titanium science and technology. Acta Mater. 61(3), 844-879.
Barlat, F., Maeda, Y., Chung, K., Yanagawa, M., Brem, J.C., Hayashida, Y., Lege, D.J., Matsui, K., Murtha, S.J., Hattori, S., Becker, R.C., Makosey, S., 1997. Yield function development for aluminum alloy sheets. J. Mech. Phys. Solids 45, 1727-1763.
Barlat, F., Brem, J. C., Yoon, J. W., Chung, K., Dick, R. E., Lege, D. J., Chu, E., 2003. Plane stress yield function for aluminum alloy sheets-part 1: theory. Int. J. Plasticity 19(9), 1297-1319.
Barlat, F., Aretz, H., Yoon, J. W., Karabin, M. E., Brem, J. C., Dick, R. E., 2005. Linear transfomation-based anisotropic yield functions. Inter. J. Plasticity, 21(5), 1009-1039.
Banabic, D., Barlat, F., Cazacu, O., Kuwabara, T., 2010. Advances in anisotropy and formability. Int. J. Mater. Forming 3(3), 165-189.
Bassani, J. L., Racherla, V., 2011. From non-planar dislocation cores to non-associated plasticity and strain bursts. Progress in Mater. Sci. 56(6), 852-863.
Boger, R.K., Wagoner, R.H., Barlat, F., Lee, M. G., Chung, K., 2005. Continuous, large strain, tension/compression testing of sheet material. Int. J. Plasticity 21(12), 2319-2343.
Bridier, F., Villechaise, P., Mendez, J., 2005. Analysis of the different slip systems activated by tension in a α/β titanium alloy in relation with local crystallographic orientation. Acta Mater. 53(3), 555-567.
Brown, D.W., Beyerlein, I.J., Sisneros, T.A., Clausen, B., Tomé, C.N., 2012. Role of twinning and slip during compressive deformation of beryllium as a function of strain rate. Int. J. Plasticity 29, 120-135.
Bulatov, V. V., Richmond, O., Glazov,M.V., 1999. An atomistic dislocation mechanism of pressure-dependent plastic flow in aluminum. Acta Mater. 47(12), 3507-3514.
Cazacu, O., Barlat, F., 2004. A criterion for description of anisotropy and yield differential effects in pressure-insensitive metals. Int. J. Plasticity 20, 2027–2045.
Cazacu, O., Plunkett, B., Barlat, F., 2006. Orthotropic yield criterion for hexagonal closed packed metals. Int. J. Plast. 22, 1171-1194.
Cazacu, O., Stewart, J. B., 2009. Analytic plastic potential for porous aggregates with matrix exhibiting tension-compression asymmetry. J. Mech. Phy. Solids 57(2), 325-341
Cheng, S., Spencer, J. A., Milligan, W. W., 2003. Strength and tension/compression asymmetry in nanostructured and ultrafine-grain metals. Acta Mater. 51(15), 4505-4518.
Deshpande, V.S., Needleman, A., Van der Giessen,E., 2005. Plasticity size effects in tension and compression of single crystals. J. Mech. Phy. Solids 53(12): 2661-2691.
Drucker, D. C.,1973. Plasticity theory strength-differential (SD) phenomenon, and volume expansion in metals and plastics. Metal. Transac. 4(3), 667-673.
Eshelby, J.D., 1957. The determination of the elastic field of an ellipsoidal inclusion, and related

problems. Proceedings of the Royal Society of London, Series A. Math. Phy. Sci. 241: 376-396.
Fundenberger J J, Philippe M J and Wagner F, et al.,1997. Modelling and prediction of mechanical properties for materials with hexagonal symmetry (zinc, titanium and zirconium alloys). Acta Mater. 45, 4041-4055.
Fitzgibbon, A., Pilu, M., Fisher, R. B., 1999. Direct least square fitting of ellipses. Pattern Analysis and Machine Intelligence, IEEE Transactions 21(5): 476-480.
Gall, K., Sehitoglu, H., Chumlyakov, Y. I., Kireeva, I. V., 1999. Tension–compression asymmetry of the stress–strain response in aged single crystal and polycrystalline NiTi. Acta Mater. 47(4), 1203-1217.
Gilles, G., Hammami, W., Libertiaux, V., Cazacu, O., Yoon, J.H., Kuwabara, T., Habraken, A.M., Duchêne, L., 2011. Experimental characterization and elastoplastic modeling of the quasi-static mechanical response of TA-6V at room temperature. Int. J. Solids Struct. 48, 1277-1289.
Graff, S., Brocks, W., Steglich, D., 2007. Yielding of magnesium: From single crystal to polycrystalline aggregates. Int. J. Plasticity 23(12), 1957-1978.
Grolleau, V., Louche, H., Delobelle, V., Penin, A., Rio, G., Liu, Y., Favier, D., 2011. Assessment of tension–compression asymmetry of NiTi using circular bulge testing of thin plates. Scripta Mater. 65(4), 347-350.
Gurao N. P., Kapoor, R. and Suwas, S., 2011. Deformation behaviour of commercially pure titanium at extreme strain rates. Acta Mater. 59: 3431-3446.
Hielscher, R., Schaeben, H., 2008. A novel pole figure inversion method: specification of the MTEX algorithm. J. Appl. Cryst. 41(6), 1024-1037.
Iadicola, M. A., Foecke, T., Banovic, S. W., 2008. Experimental observations of evolving yield loci in biaxially strained AA5754-O. Int. J. Plasticity 24(11), 2084-2101.
Jiao, F., Bettge, D., Österle, W., Ziebs, J., 1996. Tension-compression asymmetry of the (001) single crystal nickel base superalloy SC16 under cyclic loading at elevated temperatures. Acta Mater. 44(10), 3933-3942.
Jin, L., Dong, J., Sun, J., Luo, A.A., 2015. In-situ investigation on the microstructure evolution and plasticity of two magnesium alloys during three-point bending. Int. J. Plasticity 72,218-232.
Jones, I. P., Hutchinson, W. B., 1981. Stress-state dependence of slip in titanium-6Al-4V and other HCP metals. Acta Metal. 29(6), 951-968.
Jeong, Y., Barlat, F., Tomé, C. N., Wen, W., 2016. A comparative study between micro-and macro-mechanical constitutive models developed for complex loading scenarios. Inter. J. Plasticity, in press.
Kabirian, F., Khan, A.S., Gnäupel-Herlod, T., 2015. Visco-plastic modeling of mechanical responses and texture evolution in extruded AZ31 magnesium alloy for various loading conditions. Int. J. Plasticity 68, 1-20.
Khan, A.S., Kazmi, R., Farroch, B., 2007. Multiaxial and nonproportional loading responses, anisotropy and modeling of Ti-6Al-4V titanium alloy over wide ranges of strain rates and temperatures. Int. J. Plasticity 23, 931-950.
Khan, A.S., Yu, S.J., 2012. Deformation induced anisotropic responses of Ti–6Al–4V alloy. Part I: Experiments. Int. J. Plasticity 38, 1-13.
Kuwabara, T., 2007. Advances in experiments on metal sheets and tubes in support of constitutive modeling and forming simulations. Int. J. Plasticity 23, 385-419.
Lebensohn,R.A., Gonzalez,M.I., Tomé,C.N., Pochettino,A.A.,1996. Measurement and prediction of texture development during a rolling sequence of Zircaloy-4 tubes. J. Nuclear Mater. 229, 57-64.
Lebensohn, R.A., Canova, G.R., 1997. A self-consistent approach for modelling texture development of two-phase polycrystals: application to titanium alloys. Acta Mater. 45, 3687-3694.
Li, H., Yang, H., Song, F. F., Zhan, M., Li, G. J., 2012. Springback characterization and

behaviors of high-strength Ti–3Al–2.5 V tube in cold rotary draw bending. J. Mater. Process. Technol. 212(9), 1973-1987.
Li, H., Shi, K., Yang, H., 2013. 3D-FE study on deformation behaviors in cold pilgering of high strength TA18 titanium alloy tube. AIP Publishing 1532(1), 311-316.
Li, H., Hu, X., Yang, H., Li, L., 2016. Anisotropic and asymmetrical yielding and its distorted evolution: Modeling and applications. Int. J. Plasticity, 82, 127-158.
Lim, H., Hale, L.M., Zimmerman, J.A., Battaile, C.C., Weinberger, C.R., 2015. A multi-scale model of dislocation plasticity in α-Fe: Incorporating temperature, strain rate and non-Schmid effects. Int. J. Plasticity 73,100-118.
Máthis, K., Csiszár, G., Čapek, J., Gubicza, J., Clausen, B., Lukáš, P., Agnew, S. R., 2015. Effect of the loading mode on the evolution of the deformation mechanisms in randomly textured magnesium polycrystals−comparison of experimental and modeling results. Int. J. Plasticity 72,127-150.
Mitsunobu,T., Koizumi,Y., Lee, B. S., Chiba, A., 2014. Asymmetric slip trace formation in tension/compression cyclic deformation of biomedical Co–Cr–Mo–N alloy with negative stacking fault energy. Scripta Mater. 74, 52-55.
Mohr, D., Chevin, M. A., Greve, L., 2013. Deformation behavior of magnesium extrusions with strong basal texture: experiments and modeling. J. App. Mech. 80(6), 061002.
Mondal, C., Singh, A.K., Mukhopadhyay, A.K., 2013. Effects of different modes of hot cross-rolling in 7010 aluminum alloy: part II. mechanical properties anisotropy Metal. Mater. Transac. A 44, 2764-2777.
Nitz, A., Lagerpusch, U., Nembach, E., 1998. CRSS anisotropy and tension/compression asymmetry of a commercial superalloy. Acta Mater. 46(13), 4769-4779.
Nixon, M.E., Cazacu, O., Lebensohn, R.A., 2010. Anisotropic response of high-purity a-titanium: Experimental characterization and constitutive modeling. Int. J. Plasticity 26, 516-532.
Ogata, S., Li, J., Yip, S., 2002. Ideal pure shear strength of aluminum and copper. Sci. 298, 807-811.
Patra, A., Zhu, T., McDowell, D. L., 2014. Constitutive equations for modeling non-Schmid effects in single crystal bcc-Fe at low and ambient temperatures. Int. J. Plasticity 59, 1-14.
Piao,. J., Lee, K., Kim, J.H., Kim, H.Y., Chung, K., Barlat, F., Wagoner, R. H., 2012. A sheet tension/compression test for elevated temperature. Int. J. Plasticity 38, 27-46.
Proust,G.,Tomé,C.N.,Jain,A., Agnew,S.R.,2009. Modeling the effect of twinning and detwinning during strain-path changes of magnesium alloy AZ31. Int. J. Plasticity 25(5), 861-880.
Raniecki, B., Mróz, Z., 2008. Yield or martensitic phase transformation conditions and dissipation functions for isotropic, pressure-insensitive alloys exhibiting SD effect. Acta Mech. 195(1-4), 81-102.
Reedlunn,B., Churchill, C. B., Nelson, E.E., Shaw, J.A., Daly, S.H., 2014. Tension, compression, and bending of superelastic shape memory alloy tubes. J. Mech. Phy. Solids 63, 506-537.
Revil-Baudard,B., Chandola,N., Cazacu,O., Barlat,F., 2014. Correlation between swift effects and tension–compression asymmetry in various polycrystalline materials. J. Mech. Phy. Solids 70, 104-115.
Rodríguez-Galán, D., Sabirov, I., Segurado, J., 2015. Temperature and stain rate effect on the deformation of nanostructured pure titanium. Int. J. Plasticity 70, 191-205.
SAE, 2010. Titanium alloy tubing, seamless, hydraulic 3Al–2.5V, textured controlled cold worked, stress relieved. Aerospace Material Specification, AMS4956.
SAE,2013. Contractile strain ratio testing of titanium hydraulic tubing. Aerospace Material Specification, AS4076.
Salem A A, Kalidindi S R, Semiatin S L., 2005. Strain hardening due to deformation twinning in α-titanium: constitutive relations and crystal-plasticity modeling. Acta Mater. 53: 3495-3502.

Stanford, N., Geng, J., Chun, Y. B., Davies, C. H. J., Nie, J. F., Barnett, M. R., 2012. Effect of plate-shaped particle distributions on the deformation behaviour of magnesium alloy AZ91 in tension and compression. Acta Mater. 60(1), 218-228.
Styczynski, A., Hartig, C., Bohlen, J., Letzig, D., 2004. Cold rolling textures in AZ31 wrought magnesium alloy. Scripta Mater. 50, 943-947.
Suwas, S., Lahiri, I., Ray, R. K., Bhargava, S., 2003. The Knoop hardness yield locus of Ti–24Al–11Nb alloy. Mater. Letters 57(21), 3251-3256
Tari, D. G., Worswick, M.J., Ali, U,. Gharghouri, M.A., 2014. Mechanical response of AZ31B magnesium alloy: Experimental characterization and material modeling considering proportional loading at room temperature. Int. J. Plasticity 55, 247-267.
Tenckhoff, E., 2005. Review of deformation mechanisms, texture, and mechanical anisotropy in Zirconium and Zirconium base alloys. J. ASTM Inter. 4(2):383-408.
Tomar, V., Zhou, M., 2006. Tension-compression strength asymmetry of nanocrystalline α-Fe2O3+ fcc-Al ceramic-metal composites. App. Phy. Letters 88(23), 233107.
Tomé, C.N., Lebensohn, R.A., Kocks, U.F., 1991. A model for texture development dominated by deformation twinning: application to zirconium alloys. Acta Metall. Mater. 39, 2667-2680.
Tschopp, M. A., McDowell, D. L., 2007. Tension-compression asymmetry in homogeneous dislocation nucleation in single crystal copper. App. Phy. letters 90(12), 121916.
Tsuno, N., Shimabayashi, S., Kakehi, K., Rae, C. M. F., Reed, R. C., 2008. Tension/compression asymmetry in yield and creep strengths of Ni-based superalloys. Proceedings of the 11th International Symposium on Superalloys, 433-442.
Tuninetti, V., Gilles, G., Milis, O., Pardoen, T., Habraken, A.M., 2015. Anisotropy and tension-compression asymmetry modeling of the room temperature plastic response of Ti-6Al-4V. Int. J. Plasticity 67, 53-68.
Vitek, V., Mrovec, M., Bassani, J.L., 2004. Influence of non-glide stresses on plastic flow: from atomistic to continuum modeling. Mater. Sci. Eng. A 365, 31–37.
Wang, Z. Q., Beyerlein, I. J., 2011. An atomistically-informed dislocation dynamics model for the plastic anisotropy and tension-compression asymmetry of BCC metals. Int. J. Plasticity 27(10), 1471-1484.
Wheeler, R.G., Ireland, D.R., 1966. Multiaxial plastic flow of zircaloy-2 determined from hardness data. Electrochemical Technol. 4, 313-317.
Wilson, D. V.,1975. Origins of directional mechanical properties. Metals Technol. 2(1), 8-20.
Wu, X., Kalidindi, S.R., Necker, C., Salem, A.A., 2007. Prediction of crystallographic texture evolution and anisotropic stress–strain curves during large plastic strains in high purity α-titanium using Taylor-type crystal plasticity model. Acta Mater. 55, 423-432.
Xu F., Holt, R. A., Daymond, M. R., 2008. Modeling lattice strain evolution during uniaxial deformation of textured Zircaloy-2. Acta Mater. 56(14), 3672-3687.
Yang, H., Li, H., Zhang Z.Y., Zhan, M., Liu, J., Li, G.J., 2012. Advances and trends on tube bending forming technologies. Chinese J. Aeronaut. 25(1): 1-12.
Yang, L. X., Wang, Y. H., Lu, R. S., 2010. Advanced optical methods for whole field displacement and strain measurement. In: 2010 International Symposium on Optomechatronic Technologies (ISOT), 25-27.
Yapici, G.G., Karaman, L., Maier, H.J., 2006. Mechanical flow anisotropy in severely deformed pure titanium. Mater. Sci. Eng. A 434, 294-302.
Yoon, J.W., Lou, Y.S., Yoon, J., Glazoff, M.V., 2014. Asymmetric yield function based on the stress invariants for pressure sensitive metals. Int. J. Plast. 56, 184-202.
Zhou, G., Jain, M. K., Wu, P., Shao, Y., Li, D., Peng, Y., 2016. Experiment and crystal plasticity analysis on plastic deformation of AZ31B Mg alloy sheet under intermediate temperatures: how deformation mechanisms evolve. Int. J. Plasticity 79, 19-47.
Zisis, T., Giannakopoulos, A. E., 2011. Analysis of Knoop indentation strain hardening

effects. International Journal of Solids and Structures,48(22), 3217-3231.